Towards critical physics in 2+1d with U(2N)-invariant fermions

Simon Hands

Department of Physics, College of Science, Swansea University,
Singleton Park, Swansea SA2 8PP, U.K.

E-mail: S.j.hands@swansea.ac.uk

ABSTRACT: Interacting theories of N relativistic fermion flavors in reducible spinor representations in 2+1 spacetime dimensions are formulated on a lattice using domain wall fermions (DWF), for which a U(2N) global symmetry is recovered in the limit that the wall separation L_s is made large. The Gross-Neveu (GN) model is studied in the large-N limit and an exponential acceleration of convergence to the large-L_s limit is demonstrated if the usual parity-invariant mass $m\bar\psi\psi$ is replaced by the U(2N)-equivalent $im_3\bar\psi\gamma_3\psi$. The GN model and two lattice variants of the Thirring model are simulated for $N = 2$ using a hybrid Monte Carlo algorithm, and studies made of the symmetry-breaking bilinear condensate and its associated susceptibility, the axial Ward identity, and the mass spectrum of both fermion and meson excitations. Comparisons are made with existing results obtained using staggered fermions. For the GN model a symmetry-breaking phase transition is observed, the Ward identity is recovered, and the spectrum found to be consistent with large-N expectations. There appears to be no obstruction to the study of critical UV fixed-point physics using DWF. For the Thirring model the Ward identity is not recovered, the spectroscopy measurements are inconclusive, and no symmetry breaking is observed all the way up to the effective strong coupling limit. This is consistent with a critical Thirring flavor number $N_c < 2$, contradicting earlier staggered fermion results.

Contents

1 Introduction

Relativistic field theories of particles moving in the plane have received recent attention, particularly within the condensed-matter community, because of their potential role in describing the spin-liquid phase of quantum antiferromagnets [1, 2], the pseudogap phase of cuprate superconductors [3, 4], and of course low-energy electronic excitations in graphene [5]. However, they are interesting to study in their own right. Self-interacting theories of fermions are thought to exhibit an unexpectedly rich variety of ultra-violet renormalisation group fixed points [6], each yielding a new interacting continuum theory. One manifestation of the fixed points is the existence of phase transitions separating massless fermions from a phase in which a mass gap is dynamically generated; in condensed matter physics this represents a transition from a metallic to an insulating phase. Different fixed points fall in different universality classes, which depend on both the pattern of symmetry breaking and the number of interacting species N. In all cases under discussion, it should be stressed that the fermion mass is decribed by a parity-invariant term in the Lagrangian, which is most naturally written in terms of *reducible* (i.e. four-component) spinor fields.

Because the fixed points occur at strong coupling, they present a calculational challenge, exemplified by the generic power-counting non-renormalisability of the perturbative expansion in powers of g^2 for spacetime dimensionality $d > 2$, since for a four-fermi contact interaction $[g^2] = 2 - d$. At this stage it helps to be more concrete by discussing specific

examples. The Gross-Neveu (GN) model for interacting fermions in 2+1d is defined by the continuum Lagrangian density

$$\mathcal{L}_{GN} = \bar{\psi}(\partial\!\!\!/ + m)\psi - \frac{g^2}{2N}(\bar{\psi}\psi)^2, \tag{1.1}$$

where ψ is an N-flavor 4 component spinor field. The bare mass and interaction terms each reduce the global symmetry from U(2N) to U(N)⊗U(N) (see discussion below (1.2)); in addition there is a discrete $\mathbb{Z}_2$ symmetry[1] $\psi \mapsto \gamma_5\psi$, $\bar{\psi} \mapsto -\bar{\psi}\gamma_5$ which is broken by the mass term but not the interaction. Whilst a weak-coupling expansion makes no sense as stated in the previous paragraph, it is possible to develop an alternative expansion in powers of $1/N$, favouring Feynman diagrams containing closed loops, and suggesting a resummation [7]. At strong coupling $ag^2 \geq ag_c^2 \sim O(1)$ in the limit $m \to 0$, where a is a UV regulator length scale, it is found that $\mathbb{Z}_2$ symmetry is spontaneously broken by a vacuum bilinear condensate $\langle\bar{\psi}\psi\rangle \neq 0$. There is apparently no obstruction to taking a continuum limit $a \to 0$ as $g^2 \to g_c^2$ from either phase. In the resummed theory the interaction is no longer pointlike but rather mediated by exchange of a scalar degree of freedom propagating as k^{-1} in the deep Euclidean region $k \to \infty$; this anomalous scaling cannot correspond to a term in a local Lagrangian. This persists at higher order in $1/N$. Critical exponents receive $O(1/N)$ corrections, but always consistent with hyperscaling, a consequence of $1/N$-renormalisability [7, 8]. The picture suggested by the $1/N$ expansion is confirmed by numerical simulations, which observe the symmetry-breaking transition and extract critical exponents for N as small as 2 [9]–[12], or even 1 if a honeycomb lattice is used [13].

Another model of interest is the Thirring model, in which the interaction is a contact between conserved fermion currents, defined by the continuum Lagrangian density

$$\mathcal{L}_{\text{Thir}} = \bar{\psi}(\partial\!\!\!/ + m)\psi + \frac{g^2}{2N}(\bar{\psi}\gamma_\mu\psi)^2, \quad \mu = 0, 1, 2. \tag{1.2}$$

The Thirring model has the same global symmetries as N-flavor QED$_3$. The Lagrangian (1.2) is invariant under a U(2N) generated by matrices rotating the N flavors among themselves tensored with the 4 Dirac matrices $\{\mathbb{1}, \gamma_3, \gamma_5, i\gamma_3\gamma_5\}$. The parity-invariant mass term $m\bar{\psi}\psi$ is not invariant under γ_3 or γ_5 rotations, so there is an explicit breaking U(2N) →U(N)⊗U(N). Goldstone's theorem implies the spontaneous breaking of this symmetry results in $2N^2$ massless bosons, whereas there are none for the $\mathbb{Z}_2$ GN model of the previous paragraph. However, like the GN model the Thirring model has a renormalisable $1/N$ expansion [14–17], this time with a resummed vector mediating interactions between conserved currents with UV behaviour $\propto k^{-1}$. The resummation is not associated with a phase transition and the expansion can be developed for any g^2, implying the coupling is marginal. As g^2 is raised the mass M_v associated with the small-k behaviour of the vector propagator varies from $2m$ at weak coupling to $M_v^2 \sim O(m^{4-d}/g^2)$ at strong coupling [17]. As $g^2 \to \infty$ this suggests (1.2) is a theory of conserved currents interacting via massless vector exchange, in many respects similar to QED$_3$.

However, this may not be the end of the story. Dynamical mass generation through spontaneous symmetry breaking does not occur to any order in $1/N$, but for sufficiently

---

[1]Strictly a $(\mathbb{Z}_2)^2$ symmetry if γ_3 is taken into account.

large g^2 and sufficiently small N there are self-consistent solutions of Schwinger-Dyson equations which do have this property [18]–[20]. In the limit $g^2 \to \infty$ there is a critical N_c below which symmetry breaking occurs: for integer $N < N_c$ we therefore expect to find fixed points for some finite $g_c^2(N)$. The problem has also been studied using the functional renormalisation group [6, 21, 22], implying the existence of at least two distinct fixed points in the space of possible fermionic theories; however, this approach suggests the nature of the fixed-point interaction is more general than the simple "GN" or "Thirring" forms (1.1), (1.2) discussed so far, and that a more faithful description requires extra interaction terms consistent with the global symmetries in play. The Thirring model has also been studied using lattice simulations for $2 \leq N \leq 18$ [23]–[25] which confirm that a symmetry-broken phase is indeed present, that $N_c \approx 7$ [25], and that critical exponents extracted from the equation of state close to the fixed point depend sensitively on N, quite distinct from the behaviour of the GN model. Since none of these properties is accessed in a systematic weak-coupling method, the 2+1d Thirring model may well be the simplest fermionic QFT *requiring* a computational approach.

Almost all lattice feld theory studies of 2+1d fermions to date have employed the staggered fermion formulation, in which fields are described by N_s-flavor single spinor component Grassmann fields $\chi, \bar{\chi}$ defined at each site, and relativistic covariance in the long-wavelength limit ensured by including a space-dependent $\pm$ sign on each link with the defining property that the product of such factors around any elementary plaquette equals -1. Well-known algebraic transformations show that a conventional Dirac action is recovered as $a \to 0$ expressed in terms of reducible (i.e. 4-spinor) fields $\psi, \bar{\psi}$, with ψ defined not at a site but rather distributed over the 2^3 sites defining an elementary cube. Hence ψ is interpreted as describing $2N_s$ flavors of 4-component spinor [26]. However, for $a \neq 0$ the staggered formulation does not respect the expected continuum U($4N_s$) symmetry but rather a remnant U(N_s)⊗U(N_s). Within the lattice community it is widely believed that the full global symmetry is recovered in the weakly-coupled $a \to 0$ limit expected for QCD: there is no reason to believe this is also the case at a strongly-coupled fixed point. For instance, with $N = 2$ the above considerations suggest distinct breaking patterns of Z$_2$ for the GN model and U(4)→U(2)⊗U(2) for Thirring. Recent simulations performed with $N_s = 1$ staggered fermions using an efficient fermion bag algorithm, however, have found compatible critical exponents for both "GN" [11] and "Thirring" [27] lattice models, suggesting that for this minimal flavor number the two models describe the same fixed point; in other words, extra microscopic interactions forced by the lower symmetry of the staggered action [23] may be pushing both models into the same renormalisation group basin of attraction. This seems a surprising result when the models are formulated using bosonic auxiliary fields as in the following section, which is both natural for developing the 1/N expansion and required for a conventional hybrid Monte Carlo (HMC) algorithm; however when written purely in terms of $\chi, \bar{\chi}$ fields distributed over the vertices of elementary cubes, the interactions differ by only one, presumably irrelevant, term [11].

The considerations of the previous paragraph suggest staggered fermions are not adequate to capture faithfully the correct physics of a fixed point with $g_c^2 \neq 0$. An approach in which the fermions have the correct global U(2N) symmetry built in is strongly indicated.

This insight has been shared by the Jena group, who have recently applied a non-local SLAC derivative operator to the Thirring model [28]. In this paper we will apply domain wall fermions (DWF), originally devised for the study of light quarks in QCD [29, 30], and initially studied for $2+1d$ systems in [31]. The key idea is that a fictitious dimension x_3 is introduced along which fermion propagation is governed by the operator $\bar\psi\partial_3\gamma_3\psi$. The third dimension has a finite extent L_s, with open boundaries called *domain walls* at each end labelled $\pm$. The only terms coupling the walls are either proportional to the current mass m or are interactions of the GN form (1.1). Under generic conditions there are exponentially-localised zero-mode solutions of the $2+1+1d$ Dirac equation at each wall which are eigenstates of $P_\pm = \frac{1}{2}(1 \pm \gamma_3)$. It is thus plausible that $2+1d$ operators and Green functions constructed from $2+1+1d$ fields living on the walls retain the properties of a theory which is invariant under rotations of the form $e^{i\alpha\gamma_3}$. On a lattice, if the kinetic operator is chosen with a Wilson mass M of opposite sign to m, then the doubler modes generically plaguing lattice fermion formulations do not couple to normalisable modes and are hence irrelevant [29]. Moreover, in the large-L_s limit it has been shown both numerically [31] and analytically [32] that full U(2N) symmetry is recovered, i.e. $e^{i\beta\gamma_5}$ and $e^{-\delta\gamma_3\gamma_5}$ rotations also become invariances. An unanticipated bonus is that the approach to the large-L_s U(2N)-invariant limit is accelerated if instead of the hermitian $m\bar\psi\psi$ the physically equivalent, but antihermitian, mass term $im_3\bar\psi\gamma_3\psi$ is used. This playoff between the different forms of parity-invariant mass term available for reducible spinor representations in $2+1d$ has also recently been exploited in a lattice study of non-compact QED$_3$ [33].

The remainder of the paper is organised as follows. In section 2 we review the DWF formulation for $2+1d$ reducible fermions, setting out the different possible parity-invariant mass terms and the approach of the corresponding bilinear expectation values to the large-L_s limit first studied in the context of quenched QED$_3$ in [31]. Lattice versions of the GN and Thirring models using DWF are then proposed, and their simulation using an HMC algorithm outlined. While the lattice transcription of the GN model is fairly straightforward, based on a bosonic scalar auxiliary field confined to the walls [34], there are (at least) two possible ways to treat the Thirring model, one in which a vector auxiliary field A_μ is confined to the walls, and one in which A_μ is defined uniformly throughout the bulk $0 \le x_3 \le L_s$ in analogy with the treatment of gluon degrees of freedom in QCD with DWF.

Next, section 3 examines the GN gap equation in the large-N limit, which predicts a fixed point and spontaneous dynamical mass generation for $g^2 > g_c^2$. We build on the pioneering work of ref. [34] by generalising their solution to the case of the antihermitian mass term $im_3\bar\psi\gamma_3\psi$ and demonstrating an exponential improvement in convergence to the large-L_s limit as a result. The gap equation also serves as a check to simulations of the GN model with $N = 2$ presented in section 4, where results for the dynamically-generated gap $\Sigma(g^2)$ are used to monitor the approach to the large-L_s limit, and equivalence of the hermitian and antihermitian mass terms is demonstrated. The essential question of whether symmetry breaking and critical behaviour can be probed using DWF is also addressed through studies of the scalar susceptibility peaking in the vicnity of the critical point, recovery of the axial Ward identity (using a variant of the GN model with a U(1) axial symmetry), and finally for the first time the fermion propagator obtained with DWF

is used in an exploratory study of both fermion and meson masses. While no attempt is made at a full-blown characterisation of the nature of criticality, the results of this section support the physical scenario outlined above and captured in the large-N expansion [8].

In section 5 we turn attention to the Thirring model with $N = 2$, presenting results of HMC simulations of both surface and bulk models. The symmetry-breaking bilinear condensate is calculated as a function of g^2 and evidence presented that physical couplings all the way up to the strong-coupling limit are probed. Each model shows evidence for the influence of interactions, as does the auxiliary boson action, but the results differ in qualitatively important ways. Significantly, the axial Ward identity is not respected, signalling that the relation of lattice fields and parameters to the putative continuum theory is not yet under control, and that at this stage it is not yet possible to state whether surface or bulk approaches is optimal. Fermion spectroscopy in this case is hindered by large phase fluctuations, whereas meson spectroscopy requires a much larger temporal extent than the $L_t = 24$ studied here. A robust finding, however, is that there is no evidence for spontaneous symmetry breaking, i.e. our results support $\lim_{m\to 0}\langle\bar\psi\psi\rangle = 0$, on volumes and using lattice parameters where symmetry breaking is clearly observed using staggered fermions [23]. This strongly suggests that for a theory of the form (1.2), $N_c < 2$. The results are summarised and discussed in section 6, and an appendix contains technical details of the free fermion propagator using DWF, needed for the large-N calculation of section 3.

2 Formulation and simulation

First, let's define the lattice action to be studied. The fermion kinetic term uses the $2 + 1d$ domain wall operator defined in [31, 32]:

$$S_{\text{kin}} = \bar\Psi D\Psi \equiv \sum_{x,y}\sum_{s,s'} \bar\Psi(x,s)[\delta_{s,s'}D_W(x|y) + \delta_{x,y}D_3(s|s')]\Psi(y,s') + m_i S_i, \qquad (2.1)$$

where the fields $\Psi, \bar\Psi$ are four-component spinors defined in 2+1+1 dimensions. The first term D_W is the $2 + 1d$ Wilson operator defined on spacetime volume V

$$D_W(M)_{x,y} = -\frac{1}{2}\sum_{\mu=0,1,2}\left[(1-\gamma_\mu)U_\mu(x)\delta_{x+\hat\mu,y} + (1+\gamma_\mu)U_\mu^\dagger(y)\delta_{x-\hat\mu,y}\right] + (3-M)\delta_{x,y}, \quad (2.2)$$

with M the domain wall height parameter, and D_3 controls hopping along the third dimension separating the domain walls at $s = 1$ and $s = L_s$:

$$D_{3\,s,s'} = -\left[P_-\delta_{s+1,s'}(1-\delta_{s',L_s}) + P_+\delta_{s-1,s'}(1-\delta_{s',1})\right] + \delta_{s,s'}. \qquad (2.3)$$

Here the projectors $P_\pm \equiv \frac{1}{2}(1\pm\gamma_3)$ and the connection link fields U_μ will be specified more fully later, with $U_\mu \equiv 1$ for free fields. The mass term in (2.1) only involves fields on the domain walls themselves, and can be chosen as a linear combination of terms which are either hermitian:

$$m_h S_h = m_h \sum_x \bar\Psi(x,L_s)P_-\Psi(x,1) + \bar\Psi(x,1)P_+\Psi(x,L_s), \qquad (2.4)$$

or antihermitian:

$$m_3 S_3 = im_3 \sum_x \bar{\Psi}(x, L_s)\gamma_3 P_- \Psi(x, 1) + \bar{\Psi}(x, 1)\gamma_3 P_+ \Psi(x, L_s); \tag{2.5}$$

$$\text{or } m_5 S_5 = im_5 \sum_x \bar{\Psi}(x, 1)\gamma_5 P_- \Psi(x, 1) + \bar{\Psi}(x, L_s)\gamma_5 P_+ \Psi(x, L_s). \tag{2.6}$$

Next consider $2+1d$ fields $\psi, \bar{\psi}$ defined on the walls as follows:

$$\psi(x) = P_- \Psi(x, 1) + P_+ \Psi(x, L_s); \quad \bar{\psi}(x) = \bar{\Psi}(x, L_s)P_- + \bar{\Psi}(x, 1)P_+. \tag{2.7}$$

in terms of which the three mass terms are written $m_h \bar{\psi}\psi$, $im_3 \bar{\psi}\gamma_3\psi$, and $im_5 \bar{\psi}\gamma_5\psi$ respectively. The three terms are all parity-invariant and define physically equivalent ways of breaking U(2N) →U(N)⊗U(N). In ref. [31] it was demonstrated, in the context of quenched QED$_3$, that for sufficiently large L_s the three mass terms yield compatible results for the corresponding bilinear condensates $\langle \bar{\psi}\Gamma_i\psi \rangle$, with $\Gamma_i \in \{\mathbb{1}, i\gamma_3, i\gamma_5\}$, consistent with the recovery of U(2N)-invariance in this limit. Moreover, while $i\langle \bar{\psi}\gamma_3\psi \rangle$ and $i\langle \bar{\psi}\gamma_5\psi \rangle$ are numerically indistinguishable, the finite-L_s errors show a distinct hierarchy, i.e. with

$$\langle \bar{\psi}\psi \rangle_{L_s} = \langle \bar{\psi}\psi \rangle_{L_s \to \infty} + \Delta_h(L_s) + \epsilon_h(L_s);$$
$$i\langle \bar{\psi}\gamma_{3,5}\psi \rangle_{L_s} = i\langle \bar{\psi}\gamma_{3,5}\psi \rangle_{L_s \to \infty} + \epsilon_{3,5}(L_s). \tag{2.8}$$

then $\Delta_h \gg \epsilon_h \gg \epsilon_3 \equiv \epsilon_5$. The error Δ_h is defined by the imaginary part of $i\langle \bar{\psi}\gamma_3\psi \rangle$ obtained using just $\bar{\Psi}(L_s)$ and $\Psi(1)$: the fields on the opposite walls yield the conjugate. Therefore Δ_h can be estimated using measurements made with mass term $m_3 S_3$. In ref. [32] it was shown for a gauge theory that an expansion of the bilinear condensate $\langle \bar{\psi}\psi \rangle_{L_s}$ in powers of m_h/D_{L_s}, where D_{L_s} is a $2+1d$ *truncated overlap operator* proportional to the continuum Dirac operator in the large-L_s long-wavelength limit, for finite L_s generically contains even powers of m_h, whereas the corresponding expansion of $i\langle \bar{\psi}\gamma_3\psi \rangle$ only contains odd powers of m_3, a property shared with the continuum theory. Hence a residual $\Delta_h(m_h, Ls)$ with only weak dependence on m_h as $m_h \to 0$ cannot be excluded, consistent with the hierarchy reported below (2.8).

The Gross-Neveu (GN) model for interacting fermions in $2+1d$, defined by the continuum Lagrangian density (1.1) with ψ an N-flavor 4 component spinor field, exhibits spontaneous breaking of $\mathbb{Z}_2$. The model is readily generalised to exhibit spontaneous breaking of a continuous symmetry, e.g. U(1), by modifying the contact interaction to $[(\bar{\psi}\psi)^2 - (\bar{\psi}\gamma_5\psi)^2]$ — see section 4.2 below. It is convenient to reformulate (1.1) in terms of a real scalar auxiliary boson field σ:

$$\mathcal{L}_{GN\sigma} = \bar{\psi}(i\partial\!\!\!/ + m + \sigma)\psi + \frac{N}{2g^2}\sigma^2, \tag{2.9}$$

in which case symmetry breaking is signalled by $\Sigma \equiv \langle \sigma \rangle \neq 0$. Note that physically equivalent models are obtained by replacing the contact interaction of (1.1) by the U(2N)-equivalent forms $-(\bar{\psi}\gamma_3\psi)^2$, $-(\bar{\psi}\gamma_5\psi)^2$, along with masses m_3, m_5 multiplying the corresponding bilinears.

Formulation of the GN model on a lattice with DWF proceeds from the observation that the interaction with the auxiliary in (2.9) formally resembles a mass term [34]. The DWF formulation follows from (2.2) with $U_\mu \equiv 1$, (2.3), (2.4) with the interaction term defined solely in terms of fields on the domain walls,

$$S_{\text{GNint}} = \sum_x \sigma(x)[\bar{\Psi}(x, L_s)P_-\Psi(x, 1) + \bar{\Psi}(x, 1)P_+\Psi(x, L_s)], \qquad (2.10)$$

with obvious generalisations based on (2.5), (2.6). An interesting distinction with previous work is that here the auxiliary field variables are simply defined on the lattice sites; in the conventional formulation using staggered fermions σ is defined on the sites of the *dual* lattice [8].

The other interacting theory considered in this paper is the Thirring model (1.2). Again, it is convenient to recast the model using a real vector auxiliary field A_μ:

$$\mathcal{L}_{\text{Thir}} = \bar{\psi}(\slashed{\partial} + iA_\mu\gamma_\mu + m)\psi + \frac{N}{2g^2}A_\mu^2. \qquad (2.11)$$

In this latter form the formal resemblance of A_μ to an abelian gauge field is manifest, although the last term in (2.11) spoils gauge invariance. In the $1/N$ expansion A_μ interpolates a massive vector boson of mass M_v; the ratio M_v/m is governed by the coupling strength g^2 [17]. However, symmetry breaking U(2N) →U(N)⊗U(N) via generation of a bilinear condensate does not occur at any order in $1/N$.

There are several variants of lattice formulation of the Thirring model, even when using staggered fermions [23]. In the so-called *non-compact* approach the interaction between fermion bilinears and the vector auxiliary defined on the lattice links is linear; this has the virtue that only four-fermion terms are generated on integration over A_μ, making the connection with the continuum form (1.2) as transparent as possible. However, as shown in [23], this regularisation fails to preserve transversity of the vacuum polarisation term contributing to the A_μ-propagator (i.e. $\partial_\mu\Pi_{\mu\nu} = O(a^{-1})$), leading to an additive renormalisation of g^2 and consequent uncertainty in identifying the strong-coupling limit [25]. In this paper two non-compact DWF formulations are investigated. First, by analogy with (2.10) we study a *surface* formulation with $U_\mu \equiv 1$ in (2.2) and link fields $A_\mu(x)$ defined solely on the walls interacting with point-split bilinears:

$$S_{\text{surf}} = \frac{i}{2}\sum_{x,\mu} A_\mu(x)[\bar{\Psi}(x, 1)\gamma_\mu P_-\Psi(x+\hat{\mu}, 1) + \bar{\Psi}(x, L_s)\gamma_\mu P_+\Psi(x+\hat{\mu}, L_s)] \quad (2.12)$$

$$+ A_\mu(x-\hat{\mu})[\bar{\Psi}(x, 1)\gamma_\mu P_-\Psi(x-\hat{\mu}, 1) + \bar{\Psi}(x, L_s)\gamma_\mu P_+\Psi(x-\hat{\mu}, L_s)].$$

Notice in this case the interaction couples fermion fields on the same wall. Second, we push the analogy between the vector auxiliary and an abelian gauge field by defining a *bulk* interaction between an s-independent $A_\mu(x)$ and the vector bilinear current defined for all s:

$$S_{\text{bulk}} = \frac{i}{2}\sum_{x,\mu,s} A_\mu(x)[\bar{\Psi}(x, s)(-1+\gamma_\mu)\Psi(x+\hat{\mu}, s)] + A_\mu(x-\hat{\mu})[\bar{\Psi}(x, s)(1+\gamma_\mu)\Psi(x-\hat{\mu}, s)].$$

$$(2.13)$$

This differs from (2.12) on the walls by the presence of a formally-irrelevant remnant of the Wilson term (corresponding to the ± 1s in (2.13)). The relation with the gauge-invariant kinetic term (2.2) with $U_\mu = (1 + A_\mu)$ is clear. If we regard A_μ as a gauge field, then the distinction between (2.12) and (2.13) is that in the former case the $2+1+1d$ fields are exposed to s-like plaquettes carrying non-zero flux at both $s = 1$ and $s = L_s$, whereas in the latter case such plaquettes carry zero flux by construction. At strong coupling the analogy may be crude; since the effective connection is $(1 + A_\mu)$ rather than e^{iA_μ} the s-plaquettes are not constrained by unitarity, and may still fluctuate in magnitude if not in phase.

After introduction of auxiliary bosons both GN and Thirring models with DWF can be written in the form

$$S = S_{\text{kin}} + S_{\text{int}} + S_{\text{bos}} \tag{2.14}$$
$$= \sum_{i=1}^{N} \sum_{x,y} \sum_{s,s'} \bar{\Psi}^i(x,s) \mathcal{M}(x,s|y,s') \Psi^i(y,s') + S_{\text{bos}},$$

i.e. bilinear in the $2+1+1d$ fields $\Psi^i, \bar{\Psi}^i$, where explicit flavor indices are shown. For the bulk Thirring model interactions are encoded within S_{kin} and there is no separate S_{int}. The interaction S_{int} is one of (2.10), (2.12), (2.13) and the bosonic action S_{bos} is an obvious lattice generalisation of the quadratic terms in (2.9), (2.11). On the assumption that $\mathcal{M}$, $\mathcal{M}^\dagger$ describe similar physics, then the HMC algorithm may be used to simulate both models starting from the equivalent pseudofermion action

$$S = \sum_{j=1}^{N/2} \sum_{x,y} \sum_{s,s'} \Phi^{\dagger j}(x,s) (\mathcal{M}^\dagger \mathcal{M})^{-1}(x,s|y,s') \Phi^j(y,s') + S_{\text{bos}}. \tag{2.15}$$

The requirement to have a positive definite kernel means that N must be chosen even, and hence the minimal number of flavors simulable with the HMC algorithm is $N = 2$. However, in order to obtain the correct functional measure, in general it is necessary to correct for the effect of unphysical bulk fermion modes [30], so that the fermion operator coincides with a $2+1d$ overlap operator in the large-L_s limit. For U(2N)-invariant fermions this is done by including for each flavor a term $\det(D^{-1}(m_h a = 1))$ in the functional measure [32], which may be thought of as arising from integration over bosonic Pauli-Villars fields with action $\zeta^\dagger D(1)\zeta$. It is computationally efficient to use the same pseudofermion fields $\Phi, \Phi^\dagger$ for both fermions and Pauli-Villars fields, and the following action results:

$$S = \sum_{j=1}^{N/2} \sum_{x,y} \sum_{s,s'} [D^\dagger(1)\Phi^j]^\dagger(x,s) (\mathcal{M}^\dagger \mathcal{M})^{-1}(x,s|y,s')[D^\dagger(1)\Phi^j](y,s') + S_{\text{boson}}. \tag{2.16}$$

Since the GN and surface Thirring models are formulated with $U_\mu = 1$ in (2.2), the Pauli-Villars kernel $D(1)$ has no dependence on the bosonic variables, and so can be dropped with no dynamical impact. Hence in these cases the simpler form (2.15) may be used, as pointed out in [34]. For the bulk Thirring model, the action (2.16) is simulated. For all the results presented in this paper the domain wall height is chosen to be $Ma = 1$.

3 Insights from large N

One of the main questions to be addressed in this paper is how critical physics appears when DWF are used, and what is the resulting dependence on additional non-physical parameters introduced in the formulation such as L_s. The GN model provides a good starting point because critical behaviour is already manifest in the large-N approximation, and can be accessed analytically. This approach was first applied using DWF in [34]; the corresponding study for staggered fermions was performed in [8].

We start from the continuum GN model defined in (2.9). Spontaneous breaking of a Z_2 global symmetry is signalled by the development of a vacuum expectation $\Sigma = \langle \sigma \rangle$, which in the large-$N$ limit is given self-consistently by the gap equation

$$\frac{N}{g^2}\Sigma + \langle \bar{\psi}\psi \rangle = \frac{N}{g^2}\Sigma - N\mathrm{tr}(\slashed{\partial} + m + \Sigma)^{-1} = 0. \tag{3.1}$$

For DWF σ is localised on the walls according to (2.10), and the gap equation becomes

$$\frac{\Sigma_h}{g^2} = \mathrm{tr}[P_-(D^\dagger G)(1, L_s) + P_+(D^\dagger G)(L_s, 1)]; \tag{3.2}$$

the subscript h denotes that we initially focus on a hermitian interaction term, with the fermion propagator given by $D^\dagger G$, and the free fermion Green function $G(p; s, s')$ where p is a $2+1d$ momentum is derived in appendix A. Throughout this section units are defined such that $a = 1$. The first term in square brackets contains the product $D^\dagger(1, s)G(s, L_s)$. Using (A.9), (A.10) we find

$$G(p; s, L_s) = Be^{-\alpha(L_s-s)} + (P_+A_+ + P_-A_-)e^{-\alpha(L_s+s-2)} \tag{3.3}$$
$$+ (P_+A_- + P_-A_+)e^{-\alpha(L_s-s)} + A_m(e^{-\alpha(s-1)} + e^{-\alpha(2L_s-s-1)}),$$

where

$$2\cosh\alpha = \frac{1 + b^2 + \bar{p}^2}{b}; \quad \bar{p}_\mu = \sin p_\mu; \quad b(p) = 1 - M + \sum_\mu (1 - \cos p_\mu). \tag{3.4}$$

The coefficients B, $A_\pm$, A_m are given in (A.13)–(A.15) with m_h replaced by $m_h + \Sigma_h$, while

$$D^\dagger(1, s) = \theta(s-1)\theta(L_s - s)[-P_+\delta_{s,2} + (b - i\slashed{\bar{p}})\delta_{s,1} + (m_h + \Sigma_h)P_-\delta_{s,L_s}]. \tag{3.5}$$

In calculating $P_-(D^\dagger G)(1, L_s)$ and $P_+(D^\dagger G)(L_s, 1)$, terms proportional to $\slashed{\bar{p}}$ can be dropped since they vanish on tracing. The resulting gap equation is

$$\frac{\Sigma_h}{g^2} = \frac{4}{V}\sum_p \Bigg[(m_h + \Sigma_h)(B + A_+) + bA_m$$
$$+ e^{-\alpha(L_s-1)}[2(m_h + \Sigma_h)A_m + b(B + A_+ + A_-)]$$
$$+ e^{-2\alpha(L_s-1)}[(m_h + \Sigma_h)A_- + bA_m] \Bigg], \tag{3.6}$$

where the mode sum on an $L_x L_y L_t$ lattice runs over $p_{x,y} = 2\pi n_{x,y}/L_{x,y}$, $p_0 = 2\pi(n_0 + \frac{1}{2})/L_t$. Note that finite-$L_s$ corrections appear at both $O(e^{-\alpha(L_s-1)})$ and $O(e^{-2\alpha(L_s-1)})$. In the limit
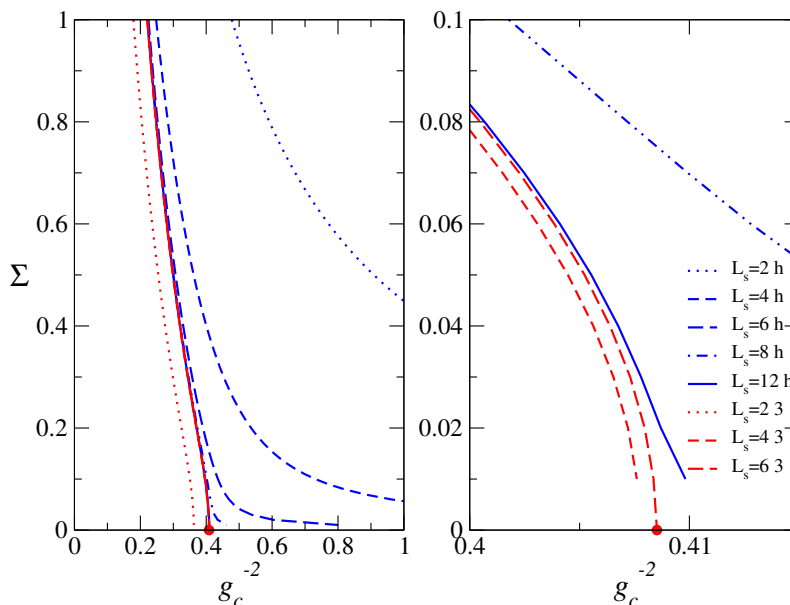
Figure 1. Solution of gap equation $\Sigma(g^2)$ on a 12^3 lattice for various L_s for both $\langle\bar\psi\psi\rangle$ (h) and $i\langle\bar\psi\gamma_3\psi\rangle$ (3) (left), and the region around the critical point enlarged (right). In all cases $m_i = 0$ and $M = 1$. The red circle denotes g_c^{-2} as given by (3.7).

$L_s \to \infty$, we take first the massless limit $m_h \to 0$ and then the limit $\Sigma \to 0$ to find the critical coupling, using (A.15):

$$\frac{1}{g_c^2} = \frac{4}{V} \sum_p \left(B + A_+ - \frac{b}{\Delta} \right). \tag{3.7}$$

The summand is given, using (3.4), by

$$B\left(1 + \frac{(e^\alpha - b)}{\Delta} \right) - \frac{b}{\Delta} = \frac{(e^\alpha - b)}{e^{2\alpha}(b - e^{-\alpha})} = \frac{z^2(p)}{\bar p^2}, \tag{3.8}$$

where the factor $z(p) = 1 - be^{-\alpha}$ was introduced in [34]. Figure 1 plots the solution to (3.6) for a 12^3 spacetime volume for various L_s. The red circle denotes the location of the transition at $g_c^{-2} = 0.408523$ from a massless phase to a phase with spontaneous mass generation given by the solution of (3.7). It can be seen that the finite-L_s corrections are significant for $L_s \lesssim 6$, and still discernable even for $L_s = 12$; note that $\Sigma_h(g^2)$ approaches the large-L_s limit from above.

With mass term proportional to m_3 the gap equation becomes $N\Sigma_3/2g^2 - i\langle\bar\psi\gamma_3\psi\rangle = 0$ and (3.3), (3.5) are replaced by

$$\begin{aligned}
G(p; s, L_s) = {} & Be^{-\alpha(L_s - s)} + (P_+ A_+ + P_- A_-)e^{-\alpha(L_s + s - 2)} \\
& + (P_+ A_- + P_- A_+)e^{-\alpha(L_s - s)} \\
& + A_{m_3}e^{-\alpha(s-1)} + A_{m_3}^* e^{-\alpha(2L_s - s - 1)}
\end{aligned} \tag{3.9}$$

and

$$D^\dagger(1, s) = \theta(s - 1)\theta(L_s - s)[-P_+\delta_{s,2} + (b - i\slashed p)\delta_{s,1} + i(m_3 + \Sigma_3)P_-\delta_{s,L_s}]. \tag{3.10}$$

– 10 –

The result is

$$\frac{\Sigma_3}{g^2} = i\mathrm{tr}[(P_-D^\dagger G)(1, L_s) - (P_+D^\dagger G)(L_s, 1)] \tag{3.11}$$

with

$$
\begin{aligned}
(P_-D^\dagger G)(1, L_s) &= [i(m_3 + \Sigma_3)(B + A_+) + bA_{m_3}] \\
&\quad + e^{-\alpha(L_s-1)}[i(m_3 + \Sigma_3)(A_{m_3} + A_{m_3}^*) + b(B + A_+ + A_-)] \\
&\quad + e^{-2\alpha(L_s-1)}[i(m_3 + \Sigma_3)A_- + bA_{m_3}^*], \tag{3.12}
\end{aligned}
$$

$$
\begin{aligned}
-(P_+D^\dagger G)(L_s, 1) &= [i(m_3 + \Sigma_3)(B + A_+) - bA_{m_3}^*] \\
&\quad + e^{-\alpha(L_s-1)}[i(m_3 + \Sigma_3)(A_{m_3} + A_{m_3}^*) - b(B + A_+ + A_-)] \\
&\quad + e^{-2\alpha(L_s-1)}[i(m_3 + \Sigma_3)A_- - bA_{m_3}], \tag{3.13}
\end{aligned}
$$

with A_{m_3} given by (A.24); the full gap equation now reads

$$
\begin{aligned}
\frac{\Sigma_3}{g^2} = \frac{4}{V}(m_3 + \Sigma_3) \sum_p \Bigg(& B + A_+ - \frac{b}{\Delta_3} \\
& + e^{-2\alpha(L_s-1)}\left[\frac{2B}{\Delta_3}\Big(e^{-2\alpha}(b - e^\alpha) + (m_3 + \Sigma_3)^2(e^{-\alpha} - b) + A_-\Big) - \frac{b}{\Delta_3}\right] \Bigg).
\end{aligned} \tag{3.14}
$$

In the large-L_s limit (3.14) coincides with (3.6), (3.7) as it must; remarkably, however, since B is free of finite-L_s corrections, and from (A.25) Δ_3 and hence $A_\pm$ only have corrections of $O(e^{-2\alpha(L_s-1)})$, we see that the gap equation (3.14) receives finite-L_s corrections only at this order; use of the twisted mass in the GN system therefore gives exponential suppression of finite-L_s corrections, as a result of cancellation of contributions with relative phase $\pm i$ between propagators running in opposite s-senses.

Solutions of (3.14) are also plotted in figure 1. As predicted, the finite-L_s corrections are much smaller, and essentially under control by $L_s = 6$. Also note $\Sigma_3(g^2)$ approaches the large-L_s limit from below. This corroborates the improved properties of the "twisted mass" formulation with respect to approaching the U(2N)-symmetric limit at large L_s, observed empirically in quenched QED$_3$ in [31], and demonstrated analytically for gauge theories in [32]. Finally, figure 2 shows the approach to the large volume limit for fixed L_s; as the volume increases the expected scaling $\Sigma_3 \propto (g_c^{-2} - g^{-2})$ is recovered in the symmetry-broken phase, consistent with the large-N critical exponent $\beta = (d - 2)^{-1} + O(1/N^2)$ [8]. As expected, finite volume effects become significant for $\Sigma_3 \lesssim L_x^{-1}$.

4 Numerical results for the Gross-Neveu model

For finite N the results of the previous section are subject to quantum corrections. In principle for the GN model these are calculable via the $1/N$ expansion, but we will use numerical simulations to address the question of what critical behaviour of DWF fermions looks like under these circumstances. The results presented in this section were obtained using a HMC algorithm based on the action (2.15) with the minimal choice $N = 2$, and $aM = 1.0$ is used throughout.
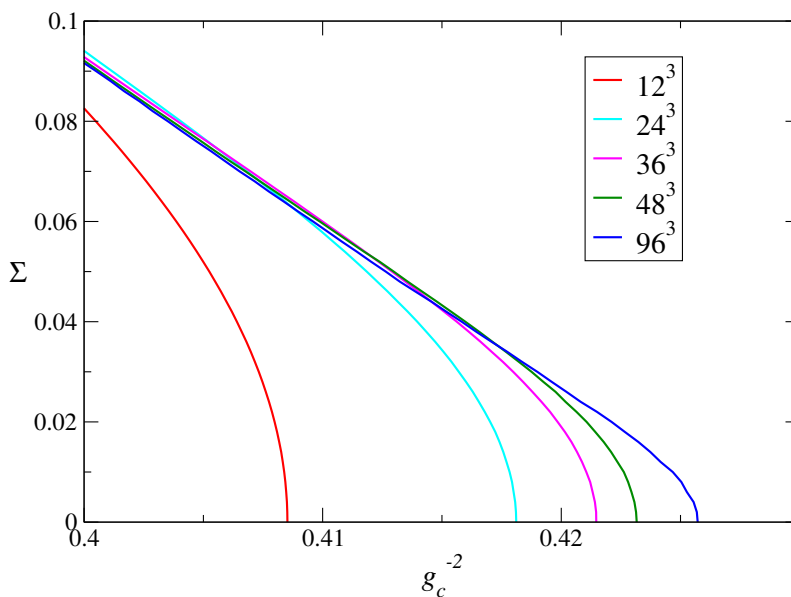
Figure 2. Solution of the gap equation $\Sigma_3(g^2)$ (3.14) for various spacetime volumes. In all cases $L_s = 12$, $m_3 = 0$ and $M = 1$.
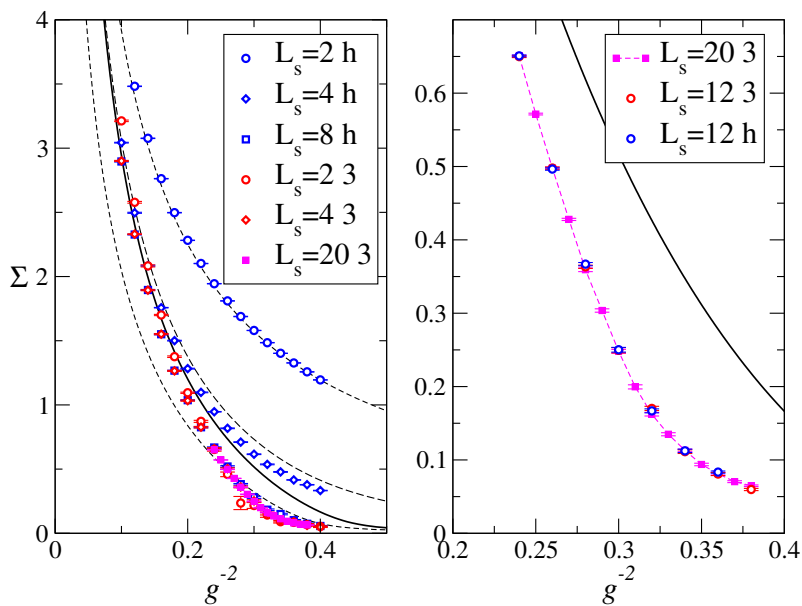

Figure 3. Results for $\Sigma_{h,3}(g^2)$ obtained on a 12^3 system for varying L_s with $am_{h,3} = 0.01$. The panel at left shows the large-N predictions of (3.6), (3.14) for $L_s = 2, 4$ for comparison, along with the large-L_s result as a full line. At right is data taken closer to the critical region with larger L_s.

4.1 Gap equation

Initially we focus on the GN model with Z_2 symmetry defined by the continuum action (2.9). The order parameter $\Sigma = \langle\sigma\rangle$ is related to the corresponding single-flavor bilinear condensate by an equation of motion $\Sigma_h = g^2\langle\bar\psi\psi\rangle$. The bilinear condensate may be estimated by stochastic means [31] at a significant numerical overhead. We have checked that the simulation respects the equation of motion, but chose to focus resources on the observable Σ. Figure 3 shows results for both Σ_h and Σ_3 as functions of g^{-2} on a $12^3 \times L_s$ system, with bare mass $am = 0.01$. For $L_s = 2$ Σ_h is in approximate agreement with the large-N result of section 3, but as L_s increases the trend is for $\Sigma(g^2)$ to fall below the large-N prediction as a result of quantum corrections. As before, the finite-L_s artifacts for Σ_3 are clearly smaller than those of Σ_h, but in this case Σ_3 approaches the large-L_s limit from above. There is fairly rapid convergence to the large-L_s limit: $\Sigma_h(L_s = 8) \approx \Sigma_3(L_s = 4)$. This can be checked in closer detail in the right panel. The $\Sigma_3(L_s = 20)$ data, shown on both panels, were obtained from 20 - 30×10^3 HMC trajectories of mean length 1.0 and can be taken to define the effective large-L_s limit. The $L_s = 12$ results for both Σ_h and Σ_3 are consistent within statistical errors.

The pronounced kink in $\Sigma_3(L_s = 20)$ seen in the right hand panel of figure 3 hints at a critical point at $ag_c^{-2} \approx 0.32$–0.34, well below the large-N value predicted by (3.7) as expected. Of course, a good estimate of g_c^{-2} requires demonstrable control over finite volume artifacts and the $m \to 0$ extrapolation, but such a simulation campaign is beyond the scope of the current study. We can note, however, that finite-N corrections are large, being O(50%) in the critical region.

The slight increase in the size of the errorbars in the critical region just discernable in figure 3 is a signal of critical fluctuations, which are more properly quantified by the susceptibility $\chi = \langle(\sigma - \langle\sigma\rangle)^2\rangle$, plotted in figure 4. The peak in the critical region signals divergence in the infinite volume massless limit, where we expect $\chi \propto |g_c^{-2} - g^{-2}|^{-\gamma}$ with $\gamma = 1 + O(1/N)$ [8]. The contrast is striking: χ_h shows no sign of critical behaviour for $L_s \leq 4$, and approaches the large-L_s limit from below, whereas χ_3 approaches the limit from above. The smallest value where the two are plausibly consistent is $L_s = 12$, but even for $L_s = 20$ there are small differences in the data. Unfortunately, the calculation is hard to control, particularly on the strong-coupling side of the transition, due to occasional brief tunnelling between true and false vacuum states related by Z_2 symmetry, which in this context should be regarded as a finite volume artifact. For this reason the actual peak height in the large-L_s limit is hard to estimate from figure 4. It appears that near criticality the susceptibility presents a more stringent challenge to reaching the large-L_s limit than the order parameter.

4.2 Axial Ward identity

Continuous global symmetries in field theories imply the existence of Ward identities relating Green functions. If we wish to check restoration of a symmetry which is formally broken at the Lagrangian level, it is important to examine the recovery of Ward identities, to check both the symmetry itself and the applicability of field identifications such as (2.7). To follow this agenda in the GN model it is necessary to enhance the model by chang-
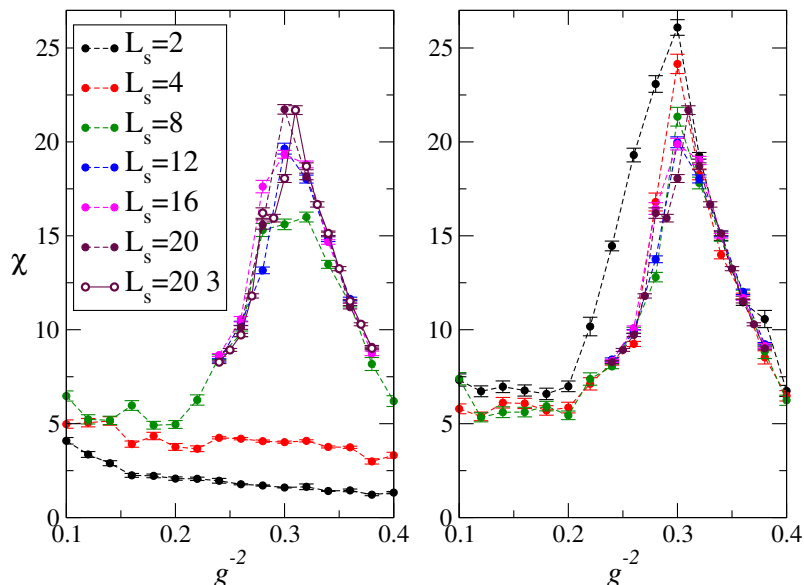
Figure 4. Results for $\chi_h(g^2)$ (left) and $\chi_3(g^2)$ (right obtained on a 12^3 system for varying L_s with $am_{h,3} = 0.01$. $\chi_3(L_s = 20)$ is plotted on both panels for comparison.

ing the broken symmetry from Z_2 to $U(1)$, requiring the introduction of a second bosonic pseudoscalar auxiliary field π. The continuum Lagrangian becomes

$$\mathcal{L}_{GN_{U(1)}} = \bar{\psi}(i\partial\!\!\!/ + m + \sigma + i\gamma_5\pi)\psi + \frac{N}{2g^2}(\sigma^2 + \pi^2), \tag{4.1}$$

and the $U(1)$ symmetry

$$\psi \mapsto e^{i\alpha\gamma_5}\psi; \quad \bar{\psi} \mapsto \bar{\psi}e^{i\alpha\gamma_5}; \quad \Phi \equiv (\sigma + i\pi) \mapsto e^{-2i\alpha}\Phi. \tag{4.2}$$

We will focus on the axial Ward identity

$$\frac{\langle\bar{\psi}\psi\rangle}{m} = N\sum_x\langle\bar{\psi}\gamma_5\psi(0)\bar{\psi}\gamma_5\psi(x)\rangle, \tag{4.3}$$

where all Green functions are normalised to just a single fermion flavor. In a symmetry broken phase with $\lim_{m\to 0}\langle\bar{\psi}\psi\rangle \neq 0$, the resulting divergence of the r.h.s. signifies the Goldstone nature of the π field. In the GN model, the Goldstone mode is dominated by disconnected fermion-line diagrams [35]. However, the auxiliary equations of motion may be used to recast the identity as

$$\Sigma = \frac{Nm}{g^2}\chi_\pi \tag{4.4}$$

where χ_π is the transverse susceptibility $\langle(\pi - \langle\pi\rangle)^2\rangle$, so all required expectation values involve solely bosonic fields. Finally, note that if instead the mass term $im_3\bar{\psi}\gamma_3\psi$ is chosen then the interaction in (4.1) takes the form $i\bar{\psi}(\gamma_3\sigma - \gamma_5\pi)\psi$, but the same Ward identity (4.4) results.
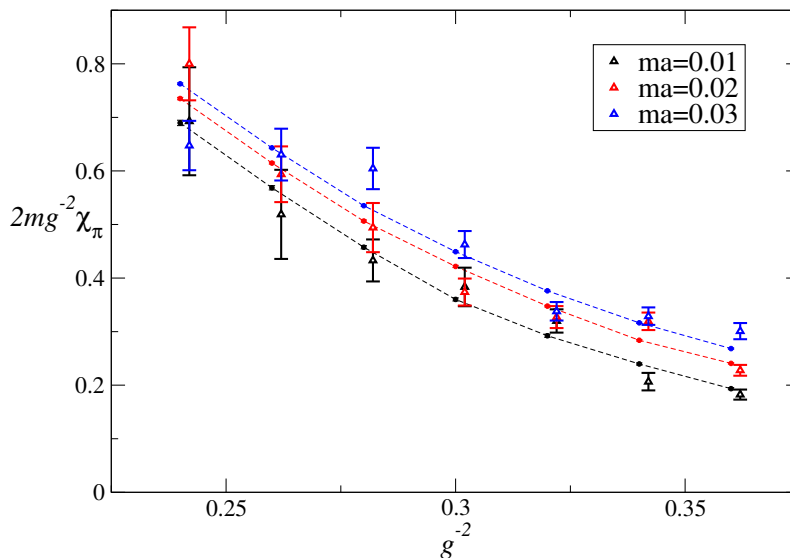
Figure 5. Plot of Σ (small symbols connected by dotted lines) and $2m\chi_\pi/g^2$ vs. g^{-2} for three values of m.

Figure 5 shows data from the $N = 2$ GN model with U(1) symmetry and mass term $m_3 S_3$ on a $12^2 \times 24$ spacetime lattice with $L_s = 8$. The data results from 30000 HMC trajectories of mean length 1.0. Each side of eq. (4.4) is plotted separately; on this scale the errors in Σ are hard to discern whereas the χ_π data suffer from large fluctuations due to the Goldstone nature of π, similar to the staggered fermion observations of [35]. Nonetheless, within the admittedly large errors the data are consistent with the Ward identity (4.4).

4.3 Spectroscopy

Finally we present some exploratory spectroscopy. Since the GN model is not constrained by Elitzur's theorem, it is possible to study the propagator of a single fermion. In addition we will examine the simplest meson correlator formed from connected fermion lines, which as shown in [31] interpolates states with $J^P = 0^\pm$. This study uses the same ensembles as section 4.2.

First consider the timeslice propagator of a free fermion with mass m_f:

$$\sum_{\vec{x}} \langle \psi(0)\bar{\psi}(x) \rangle \sim \int dp_0 \frac{e^{ip_0 x_0}}{ip_0 \gamma_0 + m_f} = P_{0\pm} e^{-m_f |x_0|}, \qquad (4.5)$$

with $P_{0\pm} \equiv \frac{1}{2}(1 \pm \gamma_0)$ and the sign chosen according to the sign of the temporal displacement x_0. Using the identification (2.7) and the identities $P_\pm P_{0+} P_\pm = \frac{1}{2}P_\pm$, $P_\mp P_{0+} P_\pm = \frac{1}{2}\gamma_0 P_\pm$,

– 15 –

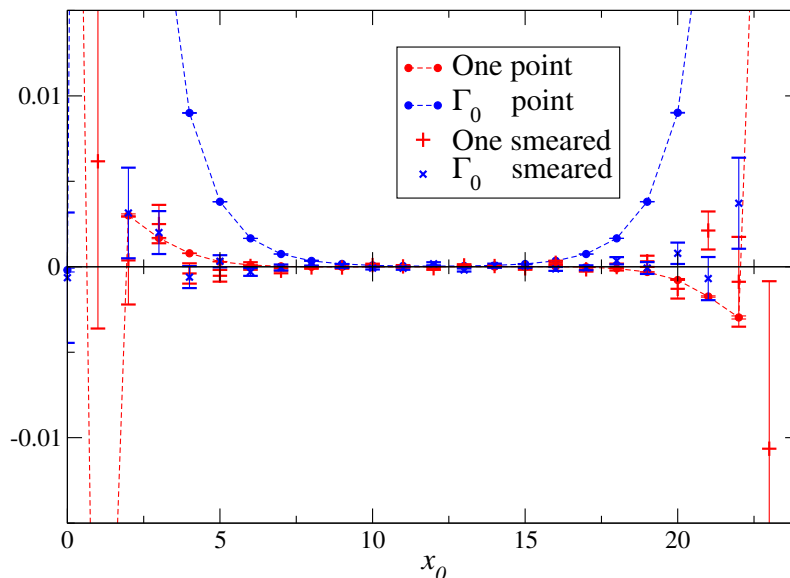**Figure 6**. Fermion timeslice correlators C_{Γ_0} and $C_{\mathbb{1}}$ evaluated on a $12^2 \times 24$ lattice with $am = 0.01$ and $L_s = 8$.

the corresponding $2+1+1d$ correlator with mass m_h and $x_0 > 0$ is

$$\mathrm{tr}P_{0+}\Big\langle (P_-\Psi(0,1) + P_+\Psi(0,L_s))(\bar{\Psi}(x,L_s)P_- + \bar{\Psi}(x,1)P_+) \Big\rangle = \qquad (4.6)$$

$$= \frac{1}{2}\mathrm{tr}\Big\langle P_-\Psi(0,1)\bar{\Psi}(x,L_s) + P_+\Psi(0,L_s)\bar{\Psi}(x,1)$$

$$+\gamma_0\Big[P_-\Psi(0,1)\bar{\Psi}(x,1) + P_+\Psi(0,L_s)\bar{\Psi}(x,L_s)\Big]\Big\rangle.$$

The generalisation to mass m_3 is straightforward. We have measured timeslice correlators using the first and third terms of the r.h.s. of (4.6) using 5 randomly-located sources on configurations separated by 5 HMC trajectories (taking care to correct for anti-periodic temporal boundary conditions when $x_{0\mathrm{sink}} < x_{0\mathrm{source}}$). They yield two distinct estimates of the fermion correlator labelled $\mathbb{1}$ (formed from $2+1+1d$ propagators linking the two domain walls) and Γ_0 (formed from propagators starting and ending on the same wall) in the following. The two should coincide in magnitude if the correlator is dominated by a simple pole of the continuum form (4.5).

Figure 6 shows the raw correlators $C_{\Gamma_0}(x_0)$ and $C_{\mathbb{1}}(x_0)$ obtained at coupling $ag^{-2} = 0.24$ using both a point source and a Gaussian smeared source

$$\eta^{\mathrm{smear}} = (1 - c + cD_\perp)^{N_{\mathrm{smear}}}\eta^{\mathrm{point}}, \qquad (4.7)$$

with $D_\perp$ the spatial part of (2.2). We chose $c = 0.25$ and $N_{\mathrm{smear}} = 10$. The essential feature is that C_{Γ_0} is even about $x_0 = L_t/2$, whereas $C_{\mathbb{1}}$ is odd, so that their linear combination is not symmetric about the centre of the lattice. Lines are drawn though the point source data to emphasise this, which also suggest the two channels don't yield
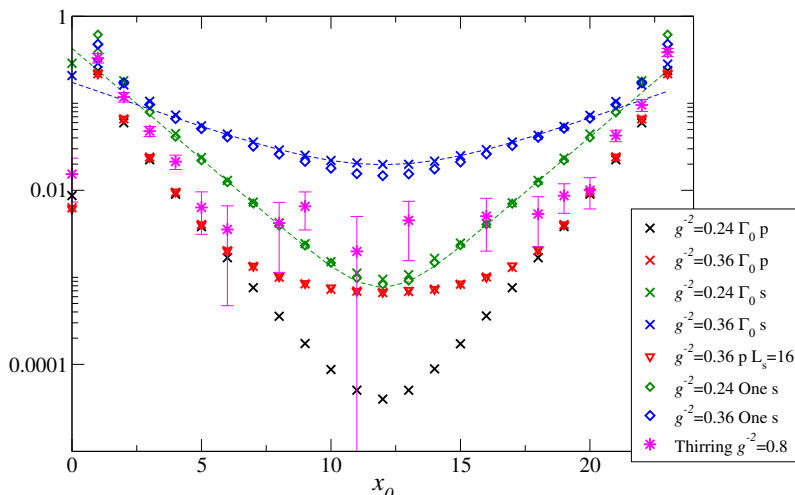
Figure 7. Timeslice correlators $\tilde{C}_{\Gamma_0}(x_0)$ and $\tilde{C}_{\mathbb{1}}(x_0)$ for $g^{-2} = 0.24$, 0.36 and $am = 0.01$. $L_s = 8$ unless otherwise indicated. Results with both point (p) and smeared (s) sources are shown. Dashed lines are simple pole fits. Also shown are Thirring model data described in section 5.

signals of equivalent magnitude. The data obtained with smeared sources has the same symmetry, but with much larger errors. These originate in the large phase fluctuations of the background auxiliary Φ field, and render the raw correlators useless for the precision fitting required by spectroscopy with the available statistics. The fluctuations also afflict the point-source data; though invisible on the scale of figure 6, the $C_{\mathbb{1}}$ datapoints actually have the wrong sign near the centre of the lattice.

The pragmatic solution adopted here is instead to study the functions $\tilde{C}_i = \sqrt{C_i^* C_i}$, effectively ignoring the phase fluctuations. It should be borne in mind that $\tilde{C}$ thus defined is not a Green function, and that any resulting particle mass estimate must strictly be a lower bound. It is also worth noting that mass fits to fermion correlators in the U(1) GN model with staggered fermions were obtained without the need for this step [36]. Results for $\tilde{C}_{\Gamma_0}$ and $\tilde{C}_{\mathbb{1}}$ for two representative couplings are plotted on a logarithmic scale in figure 7, and clearly suffer far less from fluctuations. By construction $\tilde{C}$ is symmetric about the lattice midpoint. The correlators evaluated with point sources show no coupling dependence for $|x_0| \lesssim 5$; we ascribe this to the influence at short temporal separations of excited states which are probably lattice artifacts. This is in notable contrast to using staggered fermions, where excited states are absent permitting fitting over almost the entire temporal extent, e.g. [23]. For this reason fits been made using smeared sources, which yield correlators with a better projection onto the ground state and showing a much cleaner g^{-2}-dependence; reasonable fits to a simple pole were found for $x_0 \in [6, 18]$ (Γ_0) and $x_0 \in [5, 19]$ ($\mathbb{1}$), and two such fits to $\tilde{C}_{\Gamma_0}$ are shown. Most of the data of figure 7 were obtained with $L_s = 8$ and mass term $m_h S_h$; we also show one correlator using $L_s = 16$ and $m_3 S_3$, and it is clear that at this level of accuracy the large-L_s limit is secure. The smeared source data in figure 7 also show that $\tilde{C}_{\mathbb{1}} \approx \tilde{C}_{\Gamma_0}$ over the whole x_0 range, but that there are systematic differences near the lattice midpoint, which may be a $\tilde{C}$-artifact; $C_{\mathbb{1}}$ should vanish at the lattice midpoint, and is ideally fitted with an odd function.
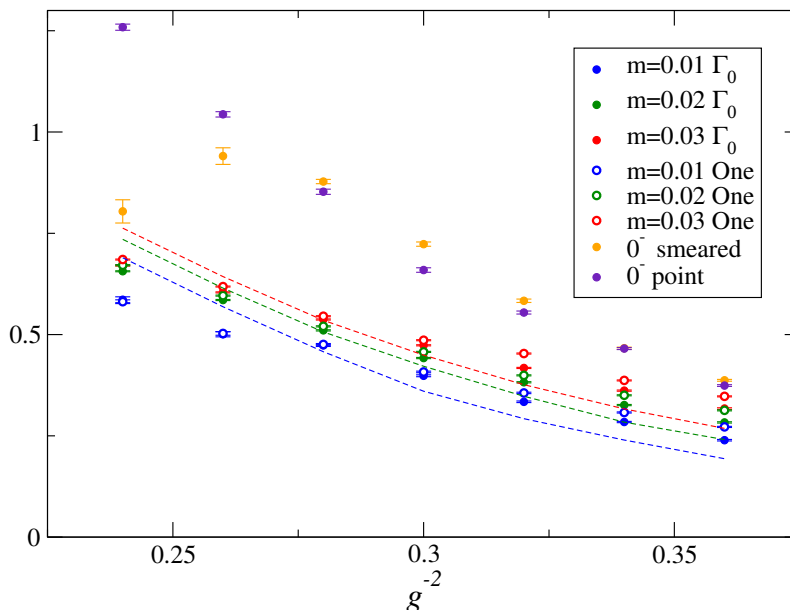
Figure 8. Spectrum of the U(1) GN model as a function of g^{-2}, showing results for the fermion using smeared sources for $am = 0.01, .02, .03$ in both Γ_0 and $\mathbb{1}$ channels, and the 0^- meson for $am = 0.01$ using both point and smeared sources. Dashed lines show the Σ data from figure 5.

Figure 8 shows results for the fermion mass m_f for $ag^{-2} \in [0.24, 0.36]$ and $am = 0.01, .02, .03$, together with the Σ data from figure 5. In the large-N limit $m_f = \Sigma + m$ [8]. The plot shows that this relation is approximately observed, but the measured m_f falls systematically below Σ at strong coupling and above Σ at weaker coupling. The fits also yield $m_{f\Gamma_0} < m_{f\mathbb{1}}$, with the trend becoming more marked at weak coupling, as might be anticipated from figure 7. Both m_f and Σ show similar variation with m over the whole range studied. Determining whether the origin of the mismatch is due to finite spatial volume, the fitted x_0-range, $O(1/N)$ corrections, or an artifact of fitting $\tilde{C}$ rather than the Green function C is beyond the scope of this exploratory study.

Figure 8 also shows mass fits to meson correlation functions, defined by the combination $C^{+-} + C^{--}$ using the notation of section 5.2 of ref. [31] (see (5.3) below), corresponding to states interpolated by the bilinears $\bar{\psi}\gamma_5\psi$ ($J^P = 0^-$), and $\bar{\psi}\gamma_3\psi$ (0^+). Again, there is evidence of significant excited state contamination (see figure 15 below), and the fits shown here were obtained from $x_0 \in [6, 18]$. There was some difficulty in obtaining stable fits at strong coupling using smeared sources, but by and large point and smeared sources yield compatible results. All the previous remarks about systematic effects apply here; the main feature revealed in figure 8 is $M_{0^\mp} \approx 2m_f$. Although the Goldstone mode has quantum numbers 0^-, it is only accessed via disconnected fermion line diagrams [35], or perhaps more effectively via the auxiliary π field as in section 4.2. Mesons formed from connected lines are only weakly bound by $O(1/N)$ effects, hence the spectrum revealed in figure 8 is physically plausible.
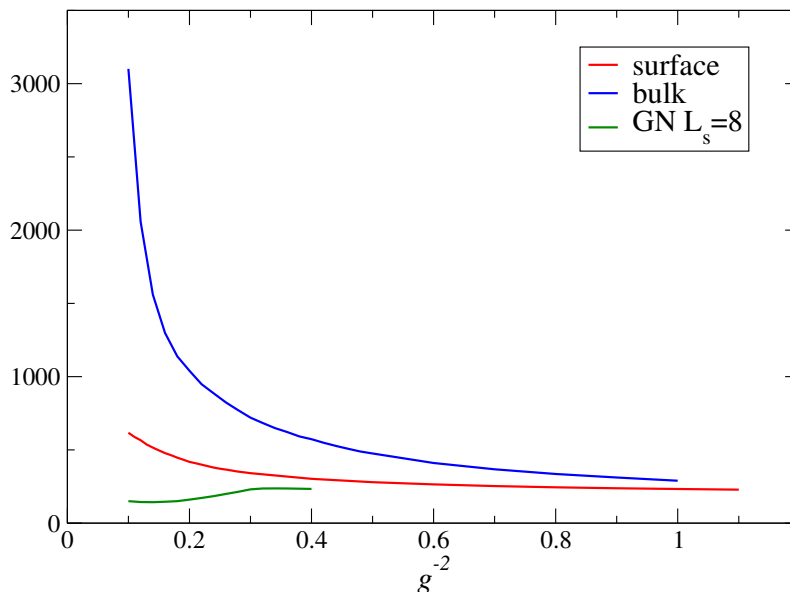
Figure 9. Number of conjugate gradient iterations needed for HMC acceptance step.

5 Numerical results for the Thirring model

Next we turn to the Thirring model, for which the bosonic auxiliary field A_μ is not simply related to a bilinear condensate order parameter, and where there is no straightforward analytic approach to compare with numerical results. Moreover as discussed in section 2 the lattice prescription is not unique. Accordingly we will explore the models defined by both surface (2.12) and bulk (2.13) interaction terms. Unless otherwise stated, the results of this section were obtained with 5000 HMC trajectories over a range of couplings g^{-2} on a 12^3 system with $L_s = 16$ and $am_3 = 0.01$, with $N = 2$ fermion flavors. The residual $\Delta_h(L_s = 16)$ defined in (2.8) ranges between 0.6–1.0×10^{-6} so the results are safely in the large-L_s limit implying $\langle\bar\psi\psi\rangle = i\langle\bar\psi\gamma_3\psi\rangle$. For reference, figure 9 plots the mean number of conjugate gradient iterations to achieve a residual norm of 10^{-9} per vector component, needed in the HMC acceptance step, for each model as a function of g^{-2}. The relative cost of the bulk model rises steeply as the coupling becomes strong. For comparison the plot also shows corresponding data for the GN model of section 4 with $L_s = 8$; here by contrast the number of iterations is maximal near the critical point.

First we simulate the surface model using the pseudofermion action (2.15). Figure 10 plots the ratio of the bilinear condensate $i\langle\bar\psi\gamma_3\psi\rangle$ to the U(2N) symmetry breaking mass m_3 for values of the coupling $ag^{-2} \in [0.1, 1.0]$. The expectation value is measured using 10 stochastic estimators every 5 HMC trajectories, as described in section 5.1 of [31]. Over the couplings explored the condensate varies by about 20%, and shows marked non-monotonic behaviour, peaking at $ag^{-2} \approx 0.2$. The plot also includes data taken with $L_s = 20$, showing that the large-L_s limit is effectively reached, and data taken on 16^3 and 20^3 systems (the latter with 2000 HMC trajectories) showing significant volume effects, though smaller than those shown in figure 2 for the large-N GN model in the critical region.
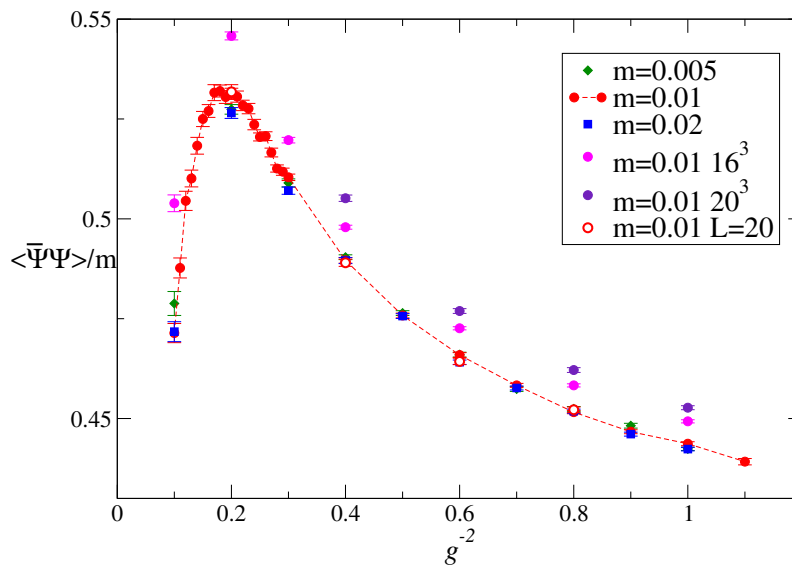
Figure 10. Bilinear condensate $i\langle\bar{\psi}\gamma_3\psi\rangle/m_3$ vs. g^{-2} for various am_3, volume, and L_s, for the surface model (2.12).
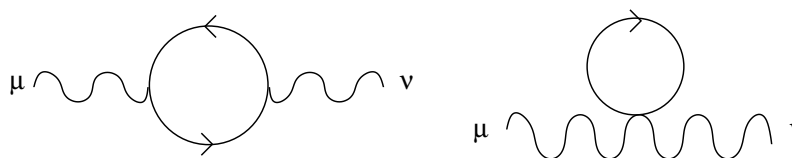

Figure 11. Leading order $1/N$ contributions to the vacuum polarisation tensor in lattice QED.

The peak in the order parameter at strong couplings has also been observed in simulations of the Thirring model with staggered fermions [23, 25]. In [23] it was observed that the fermion-auxiliary interaction fails to preserve transversity of the vector current correlator, i.e.

$$\sum_\mu \Pi_{\mu\nu}(x) - \Pi_{\mu\nu}(x - \hat{\mu}) \neq 0 \tag{5.1}$$

where $\Pi_{\mu\nu}$ is the vacuum polarisation tensor. Transversity originates in Ward-Takahashi (WT) identities arising from an underlying gauge symmetry, which on a lattice implies the link field is represented by e^{iA_μ} rather than simply A_μ. In QED$_3$ the WT identity follows from a cancellation of an $O(a^{-1})$ divergence between the two diagrams shown in figure 11. With a linearised interaction of the form (2.12) the right hand diagram is absent because there is no 2-fermion 2-boson vertex. The resulting linear divergence is absorbed by an additive renormalisation of the coupling: $g_R^{-2} = g^{-2} - J(m, N)a^{-1}$. The physical strong coupling limit $g_R^{-2} \to 0$ is thus found at non-zero g^{-2}; in practice its location must be determined by numerical simulation [25]. For $g_R^{-2} < 0$ the vector correlator in the $1/N$ expansion becomes negative, signalling violation of reflection positivity.

Now, the WT identity is independent of the details of the lattice fermion regularisation; even without a detailed calculation of the diagrams in figure 11 using DWF it is
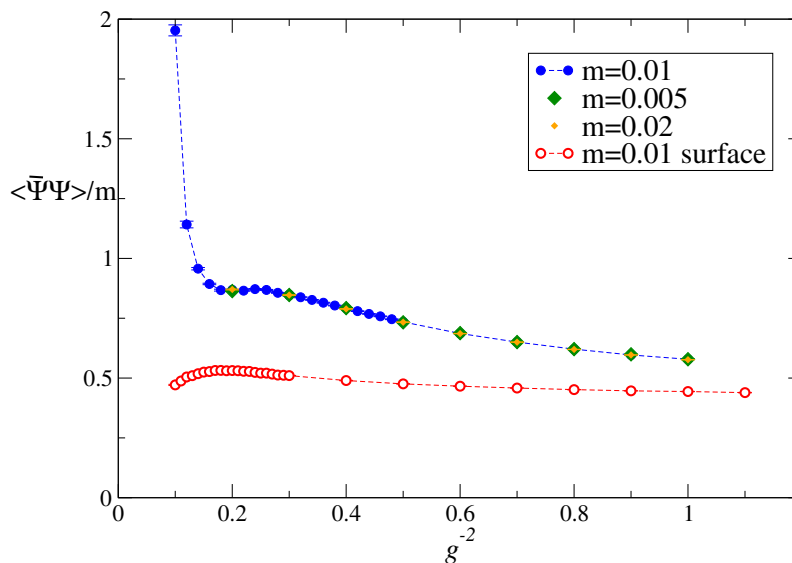
Figure 12. Bilinear condensate $i\langle\bar{\psi}\gamma_3\psi\rangle/m_3$ vs. g^{-2} for various am_3 for the bulk model (2.13). Surface model results from figure 10 are plotted for comparison.

reasonable to apply the same arguments to the current case. Hence we interpret the peak in figure 10 as evidence that the effective strong coupling limit lies at $ag^{-2} \approx 0.2$, and that the simulations have thus explored a range of couplings up to this limit. The variation of $i\langle\bar{\psi}\gamma_3\psi\rangle$ with g^{-2} shows clear evidence for interaction effects. We now observe that data taken with $am_3 = 0.005, 0.01, 0.02$ lie on top of each other, or in other words, there is no evidence to contradict the hypothesis that $\lim_{m_3\to 0} i\langle\bar{\psi}\gamma_3\psi\rangle = 0$ for all values of the coupling. This is in marked contrast with results obtained using staggered fermions on the same volume with comparable lattice parameters; compare figure 7 of ref. [23]. We conclude that a spontaneous symmetry breaking U(2N) →U(N)⊗U(N) is absent in the Thirring model defined by (2.12) for $N = 2$.

Figure 12 shows the results of a similar study for the bulk model (2.13), this time using the pseudofermion action (2.16) to perform the HMC simulation. The magnitude of $i\langle\bar{\psi}\gamma_3\psi\rangle/m_3$ is considerably larger, reflecting the fact that the two lattice models are different regularisations of a field theory. Again, there is evidence for g^{-2}-dependence, and a local maximum at $ag^2 \approx 0.2$, this time followed by a steep rise at stronger couplings. Data taken at different m_3 lie on top of each other following rescaling, once again consistent with the absence of symmetry breaking. An interesting contrast between the two formulations is highlighted in figure 13 plotting the boson action $g^{-2}A_\mu^2$ per lattice site. For non-interacting fields the expected value is $\frac{3}{2}$. In the surface model the action density stored in the auxiliary fields exceeds the free-field value and increases with coupling strength, whereas the bulk model exhibits the opposite trend, starting from the right below the free-field value and decreasing up to the effective strong coupling limit at $ag^{-2} \gtrsim 0.2$. Large UV artifacts might be expected for the expectation value of a composite operator, and indeed this is the preferred interpretation for what are ostensibly two different regularisations of the same theory. Nonetheless, the contrast between surface and bulk models may prove a useful
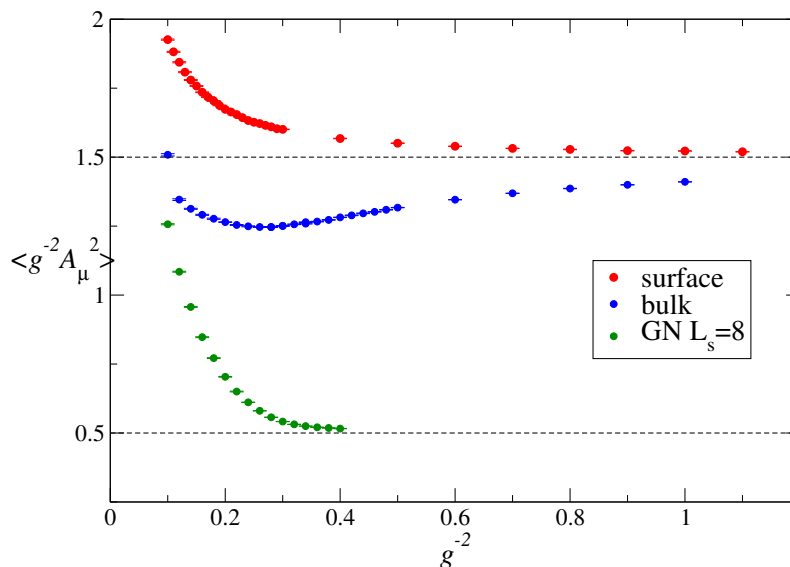
Figure 13. Auxiliary boson action $g^{-2}A_\mu^2$ for both surface and bulk models with $am_3 = 0.01$ on 12^3, and for the GN model of section 4 with $L_s = 8$. The dashed lines denote free-field values.

diagnostic. For comparison the corresponding quantity $g^{-2}\sigma^2$ is plotted for the Z_2 GN model of section 4. Here there is a clear distinction between near free-field behaviour at weak coupling and a sharp upward rise in the symmetry-broken phase, readily understood since σ is also an order parameter field.

Next consider the axial Ward identity as test of the extent to which U(2N) symmetry is restored. The equivalent identity has been found to hold in simulations of the Thirring model with staggered fermions [24]. For a $U(2N)$-invariant theory such as the Thirring model in the limit $m \to 0$, the axial Ward identity (4.3) generalises to

$$\frac{\langle\bar{\psi}_i\psi_i\rangle}{m} = \sum_{j=1}^{N}\sum_{x}\langle\bar{\psi}_i\gamma_3\psi_i(0)\bar{\psi}_j\gamma_3\psi_j(x)\rangle = \sum_{j=1}^{N}\sum_{x}\langle\bar{\psi}_i\gamma_5\psi_i(0)\bar{\psi}_j\gamma_5\psi_j(x)\rangle \equiv \chi_{\sigma,\pi}, \quad (5.2)$$

where no sum is implied by repeated explicit flavor indices. The mesons interpolated by $\bar{\psi}\gamma_3\psi$, $\bar{\psi}\gamma_5\psi$ have opposite parities. With mass term m_3, the equivalent identity has $\bar{\psi}\gamma_5\psi$ as the pseudoscalar, and the equivalent correlator contains contributions from $2+1+1d$ propagators $S(m_3; 0, s; x, s') = \langle\Psi(0,s)\bar{\Psi}(x,s')\rangle$ both running between the walls, and starting and ending on the same wall [31]:

$$\langle\bar{\psi}\gamma_5\psi(0)\bar{\psi}\gamma_5\psi(x)\rangle \equiv C_\pi^3(x) = \mathrm{tr}\Big[S(m_3; 0, L_s; x, L_s)P_- S^\dagger(m_3; 0, L_s; x, L_s)P_+$$
$$+ S(m_3; 0, 1; x, 1)P_+ S^\dagger(m_3; 0, 1; x, 1)P_-$$
$$+ S(m_3; 0, 1; x, L_s)P_- S^\dagger(m_3; 0, 1; x, L_s)P_-$$
$$+ S(m_3; 0, L_s; x, 1)P_+ S^\dagger(m_3; 0, L_s; x, 1)P_+\Big]$$
$$\equiv C^{3-+}(x) + C^{3+-}(x) + C^{3--}(x) + C^{3++}(x). \quad (5.3)$$

Assuming that only connected fermion line diagrams contribute to the Ward identity, we define the pion susceptibility $\chi_\pi = \sum_x C_\pi^3(x)$.
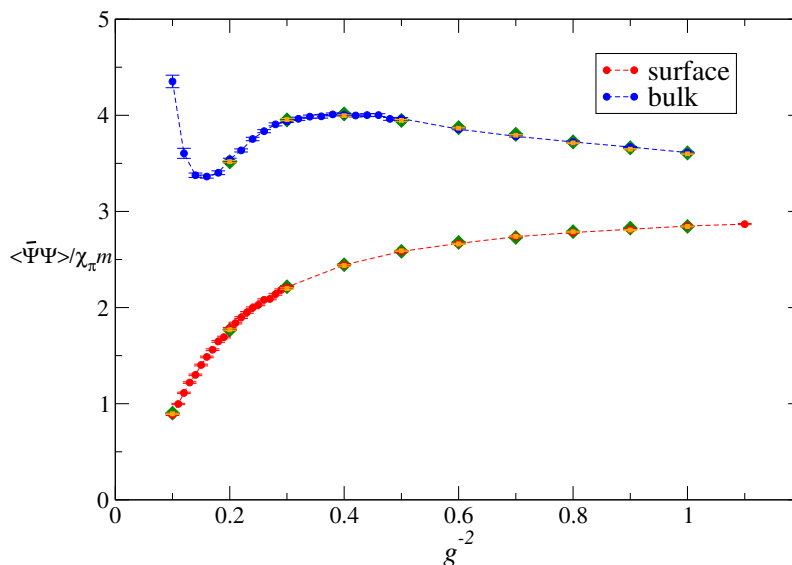
Figure 14. Ratio $i\langle\bar{\psi}\gamma_3\psi\rangle/\chi_\pi m_3$ testing axial Ward identity over a range of g^{-2} for both surface and bulk Thirring models, on $12^3 \times 16$ with $am_3 = 0.005, .01, .02$. Symbols are defined as in figure 12.

Figure 14 plots the ratio $i\langle\bar{\psi}\gamma_3\psi\rangle/m_3\chi_\pi$ as a function of g^{-2}, which should take the value unity if the axial Ward identity is preserved by the lattice formulation, for both surface and bulk models. There are clear problems both in terms of the ratio's magnitude and also its variation with g^{-2}, which is smooth but significant in the regime $g_R^{-2} > 0$. It is interesting that the trend is opposite for surface and bulk models, again suggestive that the g^{-2} variation is a UV artifact. There is no variation with m_3.

The Ward identity is not respected because the bare action (2.1), (2.12), (2.13) is not U(2N)-invariant. Possible causes of the breakdown could be that the correct fermion mass in (5.2) is not simply related to the lattice parameter m_3, or that the field identification (2.7) needs modification, resulting in renormalisation of fermion bilinears, once interactions are present. Whilst these are not fatal objections, they do make it clear that care will be needed in applying DWF techniques to this strongly-interacting system. In particular, figure 14 provides little guidance as to whether to choose bulk or surface formulations for further study. One possible way forward is instead to regard the Ward identity as a relation between renormalised quantities, so that m in (5.2) is replaced by m_f, which as a spectral quantity is much better-defined. The physical fermion mass was successfully measured in Thirring model simulations using staggered fermions [23]. To this end the fermion propagator on a $12^3 \times 24$ lattice with $L_s = 16$, $am_3 = 0.01$ was studied using 45000 HMC trajectories of the surface model, with measurements made every 5 trajectories using 5 randomly chosen sources. The best results were obtained with a smeared source (4.7) with $D_\perp$ incorporating a link connection of the form $U_\mu = e^{iA_\mu}$. The resulting $C_{\Gamma_0}(ag^{-2} = 0.8)$, where positive, is plotted in figure 7.[2] While there is a signal, the fluctuations are still too large to permit a

---

[2]The corresponding $\tilde{C}_{\Gamma_0}(x_0)$ is constant for $x_0 \gtrsim 5$, showing that in contrast to GN a correct treatment of phase fluctuations is essential to capture Thirring dynamics.
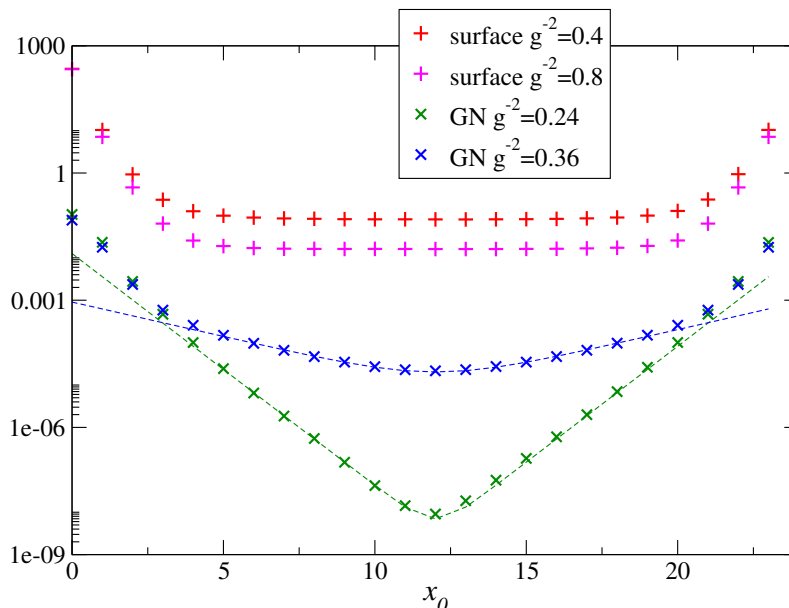
Figure 15. Meson timeslice correlators $C^{+-} + C^{--}(x_0)$ obtained with point sources for $g^{-2} = 0.4$, 0.8 for the surface Thirring model on $12^2 \times 24$ with $L_s = 8$ and $am = 0.01$. Also shown are GN model data described in section 4; dashed lines are simple pole fits.

credible fit for m_f; this may well reflect the resemblance of the Thirring model to a gauge theory, for which the correlator vanishes unless a gauge-fixing is specified.

Finally, figure 15 plots the meson correlator $C^{+-} + C^{--}$, obtained with point sources, for the surface Thirring model at two representative couplings. Corresponding results for the GN model discussed in section 4 yielding the spectrum plotted in figure 8 are shown for comparison. The contast is clear; the GN data permit a simple pole fit describing a massive meson as reported in figure 8, while the x_0-independent plateaux in the Thirring correlators are due to fermion propagators reconnecting after looping around the timelike extent of the system, and are characteristic of non-confining theories containing light fermions. Extracting spectral information in the meson channel would require lattices of much greater temporal extent than those studied here. Figure 15 provides further indirect evidence that over the coupling ranges explored dynamical fermion mass generation is happening in the GN model, but not in the Thirring model.

6 Discussion

Let us summarise the main results of the paper. The programme to apply DWF to relativistic fermions in reducible spinor representations begun in [31, 32] has been developed to cover non-perturbative simulations of interesting quantum field theories. The main results of the earlier work, namely that U(2N) global symmetries are recovered in the large-L_s limit, and that approach to the large-L_s limit is accelerated if an antihermitian or "twisted" mass term $im_3\bar{\psi}\gamma_3\psi$ is chosen, have been confirmed. The large-N solution of the GN model presented in section 3 provides a particularly nice illustration, since here the acceleration is

actually exponential. Simulations of the GN model set out in section 4 provide qualitative support for the physical picture revealed by the large-N limit, but also enable a quantification of quantum corrections of $O(1/N)$. Crucially, the results for the gap Σ and scalar susceptibility χ demonstrate that critical physics can be observed using DWF, and that finite-L_s artifacts can be controlled. Whilst a quantitative understanding of the critical properties and universal features of the fixed point theory would require simulations on a much larger scale, and in particular require much larger spacetime volumes, there is no reason to doubt the feasibility of such a campaign.

From a theoretical perspective, the principal result of the paper is that with $N = 2$ the physics of the GN and Thirring models is very different, in contradiction to results obtained with staggered fermions [11, 27]. The most obvious distinction is that the GN model exhibits a phase transition at strong-coupling to a phase in which a global symmetry (Z_2 in the example studied) is spontaneously broken and a fermion mass dynamically generated; no such transition is observed in the Thirring model despite strong evidence that the physical strong coupling limit is probed. In the GN case, subsidiary measurements of the axial Ward identity and the mass spectrum yielded results consistent with large-N expectations. This success may be due in part to the fields σ and π being related via equations of motion to bilinears of direct interest such as the order parameter field; it is certainly the case that sampling the $\{\pi\}$ ensemble is a very effective means of estimating correlators formed from disconnected diagrams. To our knowledge the measurement of the fermion correlator is the first using DWF; compared to what is known using staggered fermions, the contributions of excited state artifacts are surprisingly large, necessitating an approach based on source smearing. This in turn exacerbates the influence of phase fluctuations, so that the analysis needs to be based on the quasi-Green functions $\tilde{C}$. It is remarkable that even so the resulting spectrum shown in figure 8 matches large-N expectations as well as it does.

For the Thirring model, the non-observation of symmetry breaking is a robust result suggesting that the critical number of flavors required for dynamical symmetry breaking for the action (1.2) satisfies $N_c < 2$. If we make the additional assumption that the UV fixed point of the Thirring model coincides with the IR fixed point of QED$_3$, then this is compatible with the recent non-observation of a bilinear condensate in massless QED$_3$ with $N \geq 2$ [33]. Beyond this, by contrast, the picture is not satisfactory. Despite the inapplicability of Elitzur's theorem, phase fluctuations due to the use of smeared sources have precluded fermion spectroscopy, and small fermion masses coupled with the absence of confinement have also prevented success in meson channels. Neither failure invalidates the DWF approach; the latter is simply a problem intrinsic to studying near-conformal physics on a finite volume, while the former might in future be tackled by a form of gauge-fixing (see below). However, our inability to extract spectral information severely curtails insight into the failure of the axial Ward identity shown in figure 14, which potentially is a more profound problem, though again not necessarily fatal. What is disappointing, though, is that there is still no clear guide to the optimal lattice Thirring formulation.

Obvious future directions to explore include different formulations of the lattice Thirring model which may be less prone to the issues encountered here. Ref. [19] highlighted the role of a "hidden local symmetry" which is manifest once the Thirring action (2.11) is

supplemented by a scalar Stückelberg field ϕ coupled to A_μ. The HLS model has a gauge symmetry for which the Thirring model is the result of gauge-fixing to $\phi = 0$. Smoother gauge choices may enable better control over the fermion propagator. Formulating DWF with a true gauge symmetry will also restore transversity of the vacuum polarisation, making identification of the strong-coupling limit less ambiguous. Another route to finding and studying critical behaviour might come via implementation of the RHMC algorithm enabling $N = 1$ to be simulated. It may also be possible to find a formulation permitting $N = 1$ simulations using HMC, as recently demonstrated for QED$_3$ [33, 37]. However, a more promising route, permitted by the control offered by the DWF formulation, may be to introduce a U($2N$) and parity-invariant "Haldane" interaction term $(\bar{\psi}\gamma_3\gamma_5\psi)^2$, motivated by the findings of the functional renormalisation group [6] which identifies a significant Haldane component in the fixed-point action corresponding to the Thirring model. There is still much to learn about fermions in 2+1d.

Acknowledgments

A   Free fermion propagator

In this appendix we develop the propagator for the free DWF propagator in 2+1d following the methods set out in [38] and [39]. Inititally we consider the hermitian mass term $m_h S_h$. In 2+1d momentum space, the action may be written

$$S = \int_p \sum_{s,s'} \bar{\Psi}(p,s) D(p;s,s') \Psi(p,s') \tag{A.1}$$

where D is related to the operator D_0 defined on a lattice with infinite s-extent via

$$\begin{aligned}
D(p;s,s') &= \theta(s-1)\theta(s'-1)\theta(L_s-s)\theta(L_s-s')D_0(p;s,s') \\
&\quad + m_h(P_+\delta_{s,1}\delta_{s',L_s} + P_-\delta_{s,L_s}\delta_{s',1}),
\end{aligned} \tag{A.2}$$

with

$$\begin{aligned}
D_0 &= -(P_-\delta_{s+1,s'} + P_+\delta_{s-1,s'}) + (b(p) + i\bar{p}\!\!\!/)\delta_{s,s'}; \\
D_0^\dagger &= -(P_+\delta_{s+1,s'} + P_-\delta_{s-1,s'}) + (b(p) - i\bar{p}\!\!\!/)\delta_{s,s'}; \\
(D_0 D_0^\dagger)_{s,s'} &= \delta_{s,s'}(1 + b^2 + \bar{p}^2) - b(\delta_{s+1,s'} + \delta_{s-1,s'}),
\end{aligned} \tag{A.3}$$

and $\bar{p}_\mu$ and $b(p)$ defined in (3.4). The hermitian operator $D_0 D_0^\dagger$ has zeromodes of the form $\psi(s) = e^{\pm\alpha s}$:

$$D_0 D_0^\dagger \psi(s) = [b^2(p) + \bar{p}^2 - 2b\cosh\alpha(p) + 1]\psi(s), \tag{A.4}$$

so the zero eigenvalue condition gives the definition of α in (3.4). The Green function of $D_0 D_0^\dagger$ is given by

$$G_0(s, s') = \frac{e^{-\alpha|s-s'|}}{2b \sinh \alpha} \equiv B e^{-\alpha|s-s'|}. \tag{A.5}$$

To find the Green function of $DD^\dagger$, we need to take into account both the fact that the operators differ at $s = 1$ and $s = L_s$, and the mass term coupling the domain walls. Define

$$DD^\dagger = P_+ \Omega_+ + P_- \Omega_-; \quad G = P_+ G_+ + P_- G_-; \tag{A.6}$$

then it can be verified that

$$\begin{aligned}
\Omega_+(s, s'') G_0(s'', s') - \delta_{s,s'} = {} & B e^{-\alpha s'} e^{\alpha} (b e^{-\alpha} - 1 + m_h^2) \delta_{s,1} \\
& + B b e^{-\alpha(L_s+1)} e^{\alpha s'} \delta_{s,L_s} \\
& + B m_h b [\delta_{s,1} e^{-\alpha(L_s-s')} + \delta_{s,L_s} e^{\alpha} e^{-\alpha s'}].
\end{aligned} \tag{A.7}$$

and

$$\begin{aligned}
\Omega_+(s, s') e^{\pm \alpha s'} = {} & \delta_{s,1} e^{\pm \alpha} (b e^{\mp \alpha} - 1 + m_h^2) + m_h b \delta_{s,1} e^{\pm \alpha L_s}) \\
& + \delta_{s,L_s} (b e^{\pm \alpha(L_s+1)} + m_h b e^{\pm \alpha}).
\end{aligned} \tag{A.8}$$

The $-$ conditions are obtained using the manifest symmetry

$$\Omega_-(s, s') = \Omega_+(L_s - s + 1, L_s - s' + 1). \tag{A.9}$$

The general form of the propagator consistent with (A.9) is then

$$\begin{aligned}
G_+(s, s') = {} & G_0(s, s') + A_+ e^{-\alpha(s+s'-2)} + A_- e^{-\alpha(2L_s - s - s')} \\
& + A_m (e^{-\alpha(L_s + s - s' - 1)} + e^{-\alpha(L_s - s + s' - 1)}).
\end{aligned} \tag{A.10}$$

By requiring consistency for terms of the form $\delta_{s,1} e^{\mp s'}$, $\delta_{s,L_s} e^{\mp s'}$, the condition $\Omega_+(s, s'') G_+(s'', s') = \delta_{s,s'}$ then yields the following equations:

$$\mathcal{C} \begin{pmatrix} A_+ \\ A_m \end{pmatrix} = B \begin{pmatrix} 1 - b e^{-\alpha} - m_h^2 \\ -m_h b \end{pmatrix}; \quad \mathcal{C} \begin{pmatrix} A_m \\ A_- \end{pmatrix} = B \begin{pmatrix} -m_h b \\ -b e^{-\alpha} \end{pmatrix} \tag{A.11}$$

with

$$\mathcal{C}(m_h, L_s) = \begin{pmatrix} (b e^{\alpha} - 1 + m_h^2) + m_h b e^{-\alpha(L_s-1)} & m_h b + (b e^{-\alpha} - 1 + m_h^2) e^{-\alpha(L_s-1)} \\ m_h b + b e^{-\alpha} e^{-\alpha(L_s-1)} & b e^{\alpha} + m_h b e^{-\alpha(L_s-1)} \end{pmatrix}. \tag{A.12}$$

The solution is [39]

$$A_+ = \Delta^{-1} B (e^{\alpha} - b)(1 - m_h^2) \tag{A.13}$$

$$A_- = \Delta^{-1} B (e^{-\alpha} - b)(1 - m_h^2) \tag{A.14}$$

$$A_m = \Delta^{-1} B [-2 m_h b \sinh \alpha + e^{-\alpha(L_s-1)} (e^{-2\alpha}(b - e^{\alpha}) + m_h^2 (e^{-\alpha} - b))] \tag{A.15}$$

with

$$\Delta = b^{-1}\det\mathcal{C} = [e^{2\alpha}(b - e^{-\alpha}) + m_h^2(e^{\alpha} - b)]$$
$$+ e^{-\alpha(L_s - 1)}4m_h b\sinh\alpha \qquad\qquad (A.16)$$
$$+ e^{-2\alpha(L_s - 1)}[m_h^2(b - e^{-\alpha}) + e^{-2\alpha}(e^{\alpha} - b)].$$

Next we explore the consequences of the anti-hermitian parity-invariant mass term $m_s S_3$ (2.5) so that now

$$D(s, s') = \theta(s - 1)\theta(s' - 1)\theta(L_s - s)\theta(L_s - s')D_0(s, s')$$
$$+ im_3 P_+\delta_{s,1}\delta_{s',L_s} - im_3 P_-\delta_{s,L_s}\delta_{s',1}. \qquad (A.17)$$

Eqs. (A.7), (A.8) are replaced by

$$\Omega_+^3(s, s'')G_0(s'', s') - \delta_{s,s'} = Be^{-\alpha s'}e^{\alpha}(be^{-\alpha} - 1 + m_3^2)\delta_{s,1}$$
$$+ Bbe^{-\alpha(L_s + 1)}e^{\alpha s'}\delta_{s,L_s} \qquad\qquad (A.18)$$
$$+ iBm_3 b[\delta_{s,1}e^{-\alpha(L_s - s')} - \delta_{s,L_s}e^{\alpha}e^{-\alpha s'}]$$

and

$$\Omega_+^3(s, s')e^{\pm\alpha s'} = \delta_{s,1}e^{\pm\alpha}(be^{\mp\alpha} - 1 + m_3^2) + im_3 b\delta_{s,1}e^{\pm\alpha L_s})$$
$$+ \delta_{s,L_s}(be^{\pm\alpha(L_s + 1)} - im_3 be^{\pm\alpha}), \qquad (A.19)$$

while the symmetry (A.9) is now

$$\Omega_-(s, s') = \Omega_+^*(L_s - s + 1, L_s - s' + 1). \qquad (A.20)$$

motivating the *Ansatz*

$$G_{3+}(s, s') = G_0(s, s') + A_+ e^{-\alpha(s + s' - 2)} + A_- e^{-\alpha(2L_s - s - s')}$$
$$+ A_{m_3}e^{-\alpha(L_s + s - s' - 1)} + A_{m_3}^* e^{-\alpha(L_s - s + s' - 1)}. \qquad (A.21)$$

The consistency conditions become

$$\mathcal{C}\begin{pmatrix} A_+ \\ A_{m_3}^* \end{pmatrix} = B\begin{pmatrix} 1 - be^{-\alpha} - m_3^2 \\ im_3 b \end{pmatrix}; \quad \mathcal{C}\begin{pmatrix} A_{m_3} \\ A_- \end{pmatrix} = B\begin{pmatrix} -im_3 b \\ -be^{-\alpha} \end{pmatrix} \qquad (A.22)$$

with

$$\mathcal{C}(m_3, L_s) = \begin{pmatrix} (be^{\alpha} - 1 + m_3^2) + im_3 be^{-\alpha(L_s - 1)} & im_3 b + (be^{-\alpha} - 1 + m_3^2)e^{-\alpha(L_s - 1)} \\ -im_3 b + be^{-\alpha}e^{-\alpha(L_s - 1)} & be^{\alpha} - im_3 be^{-\alpha(L_s - 1)} \end{pmatrix}.$$
$$(A.23)$$

The solutions (A.13), (A.14) remain valid with $m \leftrightarrow m_3$ and $\Delta \leftrightarrow \Delta_3$, but now

$$A_{m_3} = \Delta_3^{-1}B[-2im_3 b\sinh\alpha + e^{-\alpha(L_s - 1)}(e^{-2\alpha}(b - e^{\alpha}) + m_3^2(e^{-\alpha} - b))] \qquad (A.24)$$

with

$$\Delta_3 = b^{-1}\det\mathcal{C} = [e^{2\alpha}(b - e^{-\alpha}) + m_3^2(e^\alpha - b)] \tag{A.25}$$
$$+e^{-2\alpha(L_s-1)}[m_3^2(b - e^{-\alpha}) + e^{-2\alpha}(e^\alpha - b)].$$

Two features are apparent: first, there are no $\mathrm{O}(e^{-\alpha L_s})$ contributions to Δ_3, so the first correction is $\mathrm{O}(e^{-2\alpha L_s})$; second, the $\mathrm{O}(e^{-\alpha L_s})$ contribution to A_{m_3} is now shifted by a phase $e^{i\frac{\pi}{2}}$ with respect to the leading order piece. Both features mitigate finite-L_s corrections to the calculation of $\langle\bar\psi\gamma_3\psi\rangle$ in the large-N GN model presented in section 3.

Open Access. This article is distributed under the terms of the Creative Commons Attribution License (CC-BY 4.0), which permits any use, distribution and reproduction in any medium, provided the original author(s) and source are credited.

References

[1] X.-G. Wen, *Quantum orders and symmetric spin liquids*, *Phys. Rev.* **B 65** (2002) 165113 [INSPIRE].

[2] W. Rantner and X.-G. Wen, *Spin correlations in the algebraic spin liquid: implications for high-T_c superconductors*, *Phys. Rev.* **B 66** (2002) 144501 [INSPIRE].

[3] I.F. Herbut, *QED$_3$ theory of underdoped high temperature superconductors*, *Phys. Rev.* **B 66** (2002) 094504 [cond-mat/0202491] [INSPIRE].

[4] Z. Tesanovic, O. Vafek and M. Franz, *Chiral symmetry breaking and phase fluctuations: a QED$_3$ theory of the pseudogap state in cuprate superconductors*, *Phys. Rev.* **B 65** (2002) 180511 [INSPIRE].

[5] A.H. Castro Neto, F. Guinea, N.M.R. Peres, K.S. Novoselov and A.K. Geim, *The electronic properties of graphene*, *Rev. Mod. Phys.* **81** (2009) 109 [INSPIRE].

[6] F. Gehring, H. Gies and L. Janssen, *Fixed-point structure of low-dimensional relativistic fermion field theories: universality classes and emergent symmetry*, *Phys. Rev.* **D 92** (2015) 085046 [arXiv:1506.07570] [INSPIRE].

[7] B. Rosenstein, B. Warr and S.H. Park, *Dynamical symmetry breaking in four Fermi interaction models*, *Phys. Rept.* **205** (1991) 59 [INSPIRE].

[8] S. Hands, A. Kocic and J.B. Kogut, *Four Fermi theories in fewer than four-dimensions*, *Annals Phys.* **224** (1993) 29 [hep-lat/9208022] [INSPIRE].

[9] L. Karkkainen, R. Lacaze, P. Lacock and B. Petersson, *Critical behavior of the three-dimensional Gross-Neveu and Higgs-Yukawa models*, *Nucl. Phys.* **B 415** (1994) 781 [*Erratum ibid.* **B 438** (1995) 650] [hep-lat/9310020] [INSPIRE].

[10] E. Focht, J. Jersak and J. Paul, *Interplay of universality classes in a three-dimensional Yukawa model*, *Phys. Rev.* **D 53** (1996) 4616 [hep-lat/9511005] [INSPIRE].

[11] S. Chandrasekharan and A. Li, *Quantum critical behavior in three dimensional lattice Gross-Neveu models*, *Phys. Rev.* **D 88** (2013) 021701 [arXiv:1304.7761] [INSPIRE].

[12] Y. Otsuka, S. Yunoki and S. Sorella, *Universal quantum criticality in the metal-insulator transition of two-dimensional interacting Dirac electrons*, *Phys. Rev.* **X 6** (2016) 011029 [arXiv:1510.08593] [INSPIRE].

[13] Z.-X. Li, Y.-F. Jiang and H. Yao, *Fermion-sign-free Majarana-quantum-Monte-Carlo studies of quantum critical phenomena of Dirac fermions in two dimensions*, *New J. Phys.* **17** (2015) 085003 [arXiv:1411.7383] [INSPIRE].

[14] G. Parisi, *The theory of nonrenormalizable interactions. 1. The large-N expansion*, *Nucl. Phys.* **B 100** (1975) 368 [INSPIRE].

[15] S. Hikami and T. Muta, *Fixed points and anomalous dimensions in O(n) Thirring model at two + ϵ dimensions*, *Prog. Theor. Phys.* **57** (1977) 785 [INSPIRE].

[16] Z. Yang, *1/N expansion and vector-fermion couplings in odd dimensions*, Texas preprint UTTG-90-40, U.S.A. (1990) [INSPIRE].

[17] S. Hands, *0(1/N_f) corrections to the Thirring model in 2 < d < 4*, *Phys. Rev.* **D 51** (1995) 5816 [hep-th/9411016] [INSPIRE].

[18] M. Gomes, R.S. Mendes, R.F. Ribeiro and A.J. da Silva, *Gauge structure, anomalies and mass generation in a three-dimensional Thirring model*, *Phys. Rev.* **D 43** (1991) 3516 [INSPIRE].

[19] T. Itoh, Y. Kim, M. Sugiura and K. Yamawaki, *Thirring model as a gauge theory*, *Prog. Theor. Phys.* **93** (1995) 417 [hep-th/9411201] [INSPIRE].

[20] M. Sugiura, *Fermion mass generation in the D-dimensional Thirring model as a gauge theory*, *Prog. Theor. Phys.* **97** (1997) 311 [hep-th/9611198] [INSPIRE].

[21] H. Gies and L. Janssen, *UV fixed-point structure of the three-dimensional Thirring model*, *Phys. Rev.* **D 82** (2010) 085018 [arXiv:1006.3747] [INSPIRE].

[22] L. Janssen and H. Gies, *Critical behavior of the (2 + 1)-dimensional Thirring model*, *Phys. Rev.* **D 86** (2012) 105007 [arXiv:1208.3327] [INSPIRE].

[23] UKQCD collaboration, L. Del Debbio, S.J. Hands and J.C. Mehegan, *The three-dimensional Thirring model for small N_f*, *Nucl. Phys.* **B 502** (1997) 269 [hep-lat/9701016] [INSPIRE].

[24] L. Del Debbio and S.J. Hands, *The three-dimensional Thirring model for N_f = 4 and N_f = 6*, *Nucl. Phys.* **B 552** (1999) 339 [hep-lat/9902014] [INSPIRE].

[25] S. Christofi, S. Hands and C. Strouthos, *Critical flavor number in the three dimensional Thirring model*, *Phys. Rev.* **D 75** (2007) 101701 [hep-lat/0701016] [INSPIRE].

[26] C. Burden and A.N. Burkitt, *Lattice fermions in odd dimensions*, *Europhys. Lett.* **3** (1987) 545 [INSPIRE].

[27] S. Chandrasekharan and A. Li, *Fermion bags, duality and the three dimensional massless lattice Thirring model*, *Phys. Rev. Lett.* **108** (2012) 140404 [arXiv:1111.7204] [INSPIRE].

[28] D. Schmidt, B. Wellegehausen and A. Wipf, *Critical flavour number of the Thirring model in three dimensions*, PoS(LATTICE 2015)050 [arXiv:1511.00522] [INSPIRE].

[29] D.B. Kaplan, *A method for simulating chiral fermions on the lattice*, *Phys. Lett.* **B 288** (1992) 342 [hep-lat/9206013] [INSPIRE].

[30] V. Furman and Y. Shamir, *Axial symmetries in lattice QCD with Kaplan fermions*, *Nucl. Phys.* **B 439** (1995) 54 [hep-lat/9405004] [INSPIRE].

[31] S. Hands, *Domain wall fermions for planar physics*, *JHEP* **09** (2015) 047 [arXiv:1507.07717] [INSPIRE].

[32] S. Hands, *From domain wall to overlap in* $2 + 1d$, *Phys. Lett.* **B 754** (2016) 264 [arXiv:1512.05885] [INSPIRE].

[33] N. Karthik and R. Narayanan, *No evidence for bilinear condensate in parity-invariant three-dimensional QED with massless fermions*, *Phys. Rev.* **D 93** (2016) 045020 [arXiv:1512.02993] [INSPIRE].

[34] P. Vranas, I. Tziligakis and J.B. Kogut, *Fermion scalar interactions with domain wall fermions*, *Phys. Rev.* **D 62** (2000) 054507 [hep-lat/9905018] [INSPIRE].

[35] I. Barbour, S. Hands, J.B. Kogut, M.-P. Lombardo and S. Morrison, *Chiral symmetry restoration and realization of the Goldstone mechanism in the* U(1) *Gross-Neveu model at nonzero chemical potential*, *Nucl. Phys.* **B 557** (1999) 327 [hep-lat/9902033] [INSPIRE].

[36] S. Hands, S. Kim and J.B. Kogut, *The* U(1) *Gross-Neveu model at nonzero chemical potential*, *Nucl. Phys.* **B 442** (1995) 364 [hep-lat/9501037] [INSPIRE].

[37] N. Karthik and R. Narayanan, *Scale-invariance of parity-invariant three-dimensional QED*, *Phys. Rev.* **D 94** (2016) 065026 [arXiv:1606.04109] [INSPIRE].

[38] Y. Shamir, *Chiral fermions from lattice boundaries*, *Nucl. Phys.* **B 406** (1993) 90 [hep-lat/9303005] [INSPIRE].

[39] P.M. Vranas, *Chiral symmetry restoration in the Schwinger model with domain wall fermions*, *Phys. Rev.* **D 57** (1998) 1415 [hep-lat/9705023] [INSPIRE].